more inert host and hence a loss in activity. However, there are now many experimental and theoretical examples of metal alloys under realistic conditions in which the more active element is stabilized at the surface by adsorbates (*21*, *30–32*). This adsorbate-induced reverse segregation effect is understood in terms of the adsorbate binding more strongly to the element, which would normally segregate to the bulk and result in a reversal of the surface segregation behavior (*21*). In the case of the Cu/Pd system, the stabilization resulting from segregation of Cu to the surface is small (0.02 eV) (*31*) compared with the ~0.4-eV increase in binding of H to Pd versus Cu (*6*, *20*). The fact that Pd segregation to the Cu surface has been observed experimentally in Pd/Cu catalysts under realistic hydrogenation operating conditions bodes well for the utility of this atomic geometry in real catalysts (*32*).

References and Notes

1. S. Abbet *et al.*, *J. Am. Chem. Soc.* **122**, 3453 (2000).
2. J. C. Fierro-Gonzalez, V. A. Bhirud, B. C. Gates, *Chem. Commun.* **42**, 5275 (2005).
3. Y. Zhai *et al.*, *Science* **329**, 1633 (2010).
4. J. M. Thomas, Z. Saghi, P. L. Gai, *Top. Catal.* **54**, 588 (2011).
5. F. Besenbacher *et al.*, *Science* **279**, 1913 (1998).
6. H. L. Tierney, A. E. Baber, J. R. Kitchin, E. C. H. Sykes, *Phys. Rev. Lett.* **103**, 246102 (2009).
7. D. O. Bellisario *et al.*, *J. Phys. Chem. C* **113**, 12863 (2009).
8. H. L. Tierney, A. E. Baber, E. C. H. Sykes, *J. Phys. Chem. C* **113**, 7246 (2009).
9. Methods and additional data are available as supporting material on *Science* Online.
10. A. Bach Aaen, E. Lægsgaard, A. V. Ruban, I. Stensgaard, *Surf. Sci.* **408**, 43 (1998).
11. T. Kammler, J. Küppers, *J. Chem. Phys.* **111**, 8115 (1999).
12. I. S. Chopra, S. Chaudhuri, J. F. Veyan, Y. J. Chabal, *Nat. Mater.* **10**, 884 (2011).
13. A. Wittstock, V. Zielasek, J. Biener, C. M. Friend, M. Bäumer, *Science* **327**, 319 (2010).
14. L. J. Lauhon, W. Ho, *Phys. Rev. Lett.* **85**, 4566 (2000).
15. T. Mitsui, M. K. Rose, E. Fomin, D. F. Ogletree, M. Salmeron, *Nature* **422**, 705 (2003).
16. G. Anger, A. Winkler, K. D. Rendulic, *Surf. Sci.* **220**, 1 (1989).
17. G. E. Gdowski, T. E. Felter, R. H. Stulen, *Surf. Sci.* **181**, L147 (1987).
18. C. Sousa, V. Bertin, F. Illas, *J. Phys. Chem. B* **105**, 1817 (2001).
19. A. Roudgar, A. Groß, *Surf. Sci.* **597**, 42 (2005).
20. J. Greeley, M. Mavrikakis, *J. Phys. Chem. B* **109**, 3460 (2005).
21. J. Greeley, M. Mavrikakis, *Nat. Mater.* **3**, 810 (2004).
22. J. Knudsen *et al.*, *J. Am. Chem. Soc.* **129**, 6485 (2007).
23. O. Skoplyak, M. A. Barteau, J. G. Chen, *J. Phys. Chem. B* **110**, 1686 (2006).
24. S. Alayoglu, A. U. Nilekar, M. Mavrikakis, B. Eichhorn, *Nat. Mater.* **7**, 333 (2008).
25. J. T. Roberts, R. J. Madix, *J. Am. Chem. Soc.* **110**, 8540 (1988).
26. W. T. Tysoe, G. L. Nyberg, R. M. Lambert, *Chem. Commun.* **11**, 623 (1983).
27. G. Kyriakou, J. Kim, M. S. Tikhov, N. Macleod, R. M. Lambert, *J. Phys. Chem. B* **109**, 10952 (2005).
28. B. Brandt *et al.*, *J. Phys. Chem. C* **112**, 11408 (2008).
29. H.-L. Jiang, Q. Xu, *J. Mater. Chem.* **21**, 13705 (2011).
30. F. Tao *et al.*, *Science* **322**, 932 (2008).
31. D. Priyadarshini *et al.*, *J. Phys. Chem. C* **115**, 10155 (2011).
32. J. A. Anderson, M. Fernández-García, G. L. Haller, *J. Catal.* **164**, 477 (1996).

An Impactor Origin for Lunar Magnetic Anomalies

Mark A. Wieczorek,[1]* Benjamin P. Weiss,[2] Sarah T. Stewart[3]

The Moon possesses strong magnetic anomalies that are enigmatic given the weak magnetism of lunar rocks. We show that the most prominent grouping of anomalies can be explained by highly magnetic extralunar materials from the projectile that formed the largest and oldest impact crater on the Moon: the South Pole–Aitken basin. The distribution of projectile materials from a model oblique impact coincides with the distribution of magnetic anomalies surrounding this basin, and the magnetic properties of these materials can account for the intensity of the observed anomalies if they were magnetized in a core dynamo field. Distal ejecta from this event can explain the origin of isolated magnetic anomalies far from this basin.

Beginning with the Apollo era, spacecraft observations have shown that portions of the lunar crust are strongly magnetized (*1–4*), yet their origin has remained unresolved. The lithologies of the source rocks for these anomalies are unknown, their time of magnetization acquisition is poorly constrained, and it is unclear whether the magnetization process was thermoremanent or shock-related (*5*, *6*). As a result, the origin of the magnetizing fields is a matter of debate, with possibilities including a core dynamo, transient fields generated during impacts, and the amplification of ambient fields by impact-generated plasmas (*7–13*).

A key difficulty is that most lunar magnetic anomalies have not been recognized to correlate with known geologic structures. A few impact basins possess central magnetic anomalies (*12*, *14*, *15*), but these anomalies are typically weak and are not representative of the most intense anomalies, most of which are located on the far side of the Moon (Fig. 1). Impact basin ejecta deposits are statistically somewhat more magnetic than other geologic units, but the magnetic signatures of the ejecta from any given basin are quite variable (*16*). A few prominent anomalies on the far side of the Moon are located near the antipodes of four young impact basins (*2*, *3*), suggestive of an exotic impact origin (*17*), but many strong anomalies are not associated with basin antipodes, and most basins do not possess antipodal anomalies.

It is also difficult to reconcile the strengths of these anomalies with the magnetic properties of known endogenous lunar materials. This is because lunar materials are very weakly magnetic relative to terrestrial materials: The saturation remanent magnetizations of mare basalts and pristine highlands rocks are weaker than those of mid-ocean ridge basalt by two to four or more orders of magnitude (*18*, *19*). To demonstrate this, we calculated the thickness of magnetized materials required to generate a representative 10-nT anomaly at an altitude of 30 km as a function of the magnetizing field strength and rock thermoremanence susceptibility (ratio of thermoremanence to the magnetizing field) (Fig. 2). The thermoremanence susceptibility correlates with both the abundance of magnetic carriers in the rock and the rock's saturation remanent magnetization (supporting online material), and lunar paleomagnetic studies imply ancient field strengths between ~1 and 120 µT (*5*, *20*, *21*). We find that even the highest postulated paleofield strengths would require extremely thick deposits of unidirectionally magnetized materials to account for the lunar magnetic anomalies. For example, more than 100 km of pristine feldspathic highland rocks would be required, but these thicknesses are greater than the thickness of the entire lunar crust. More than 10 km of mare basalts would be required, but this far exceeds the thickness of most maria (*11*). Even the relatively highly magnetic mafic impact melts, most of which are thought to be derived from the Imbrium impact event (*22*), would require thicknesses of at least several kilometers, but none of the magnetic anomalies show the topographic expressions that might be expected for such locally thick ejecta deposits.

However, there is a major geologic structure that correlates with some of the largest lunar magnetic anomalies and that has received little consideration previously. The far-side hemisphere of the Moon hosts the largest known unequivocal

[1]Institut de Physique du Globe de Paris, Université Paris Diderot, 94100 Saint-Maur des Fossés, France. [2]Department of Earth, Atmospheric, and Planetary Sciences, Massachusetts Institute of Technology, Cambridge, MA 02139, USA. [3]Department of Earth and Planetary Sciences, Harvard University, Cambridge, MA 02138, USA.

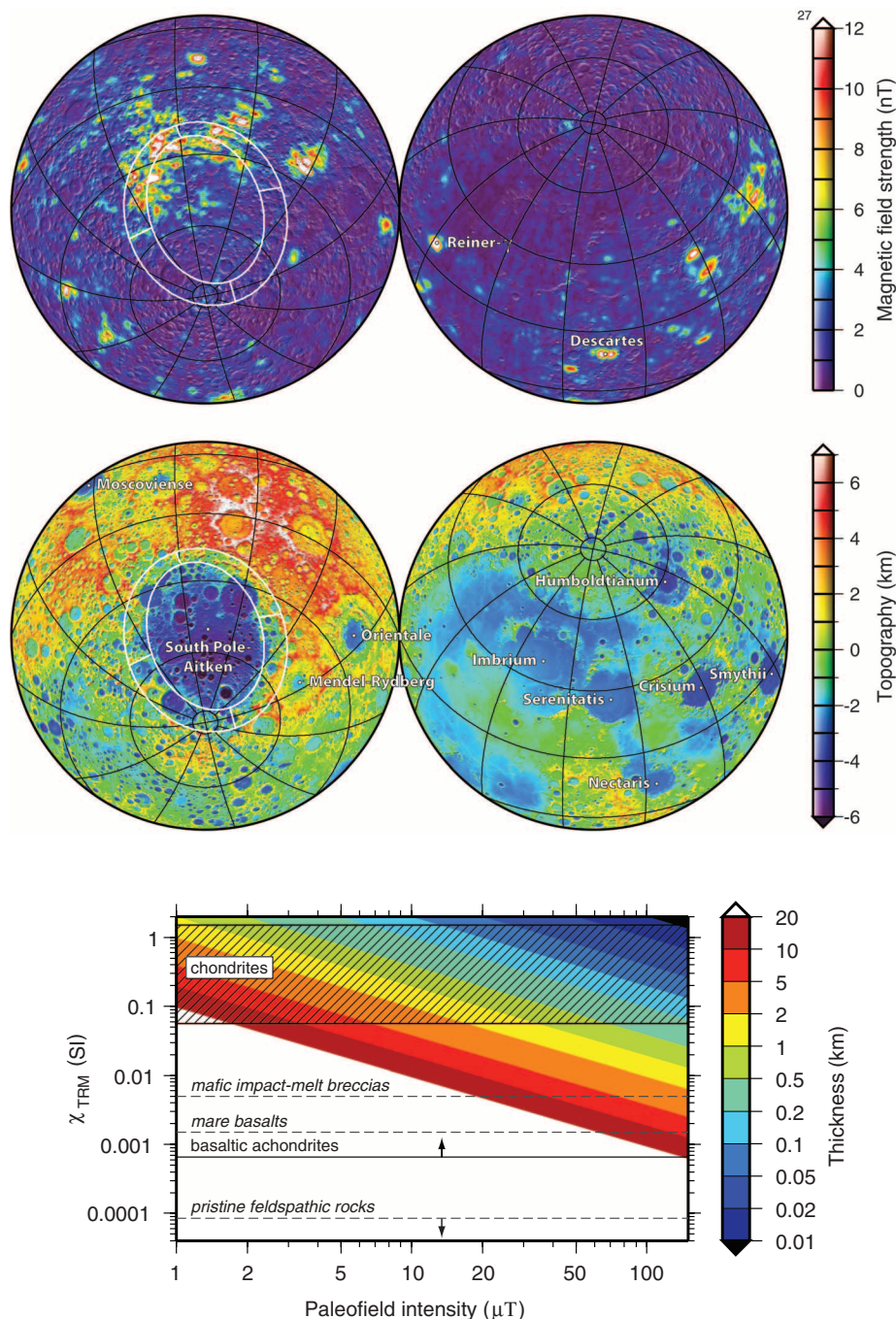*To whom correspondence should be addressed. E-mail: wieczor@ipgp.fr

Fig. 1. Magnetic field strength and topography centered over the South Pole–Aitken basin (left) and opposite hemisphere of the Moon (right). Upper panel: Total magnetic field strength from the sequential Lunar Prospector model of (*4*) evaluated 30 km above the surface. Lower panel: Topography from Lunar Reconnaissance Orbiter laser altimeter data (*34*). Ellipses elongated in the north-south direction denote the inner basin floor and outer structural rim of the South Pole–Aitken basin (*23*), and the connecting lines join the respective semiminor and semimajor axes. All images show half of the lunar surface and are displayed in a Lambert azimuthal equal-area projection overlain by a shaded relief map derived from the surface topography.

Fig. 2. Thickness of magnetic materials required to generate a 10-nT anomaly 30 km above the lunar surface. Thermoremanent magnetizations acquired in a dipolar field were determined for each thermoremanence susceptibility, χ_{TRM} (in SI units), and surface paleofield intensity within a representative disk 60 km in diameter at 30° latitude. The maximum magnetic field strength scales linearly with disk thickness, and the disk thicknesses would differ by a factor of ~2 for anomalies located at the poles and equator, or for disk diameters of 35 and 200 km. Representative thermoremanence susceptibilities of lunar (dashed) and meteoritic (solid) materials are denoted by horizontal lines (data from tables S2 and S3).

are on average about two orders of magnitude more magnetic than endogenous lunar crustal materials (Fig. 2). If the projectile was similar to a chondritic meteorite, and if these materials were magnetized by cooling in a steady core dynamo field, integrated thicknesses of only a few hundred meters would be required to account for the strength of the lunar anomalies. If the projectile was instead differentiated, the projectile core materials would have been even more magnetic than undifferentiated chondritic meteorites.

Projectile materials should be incorporated into impact deposits in abundances sufficient to substantially change the magnetic properties of these rocks. Terrestrial impact melts are known to contain materials from the impactor ranging from less than 1 weight percent (wt%) up to several wt% (*24*, *25*). The mafic impact melts sampled during the Apollo missions are thought to have formed during one or more basin-forming impact events (primarily Imbrium) and contain ~1 to 2 wt% macroscopic metallic iron that was derived from the core of a differentiated planetesimal (*22*, *26*). Given the enormous size of the South Pole–Aitken basin, the projectile that formed this basin would have been ~10 times as massive as that which formed the next largest lunar basin, and comparable in mass to all other basin-forming projectiles combined. Numerical simulations show that most of the projectile would accrete to the Moon in a molten or partially molten state for an average impact angle and velocity (*27*).

impact structure in the solar system: the South Pole–Aitken basin (Fig. 1). With a mean diameter of ~2200 km, this basin is elongated in the north-south direction and was likely formed by an oblique impact, with the projectile coming from either the north or south (*23*). The most prominent grouping of lunar magnetic anomalies coincides with the northern rim of this basin, pre-

cisely where one would expect projectile materials to have been deposited if the impact direction was from the south.

We propose that materials from the South Pole–Aitken impactor are the source materials for many of the largest lunar magnetic anomalies. With high concentrations of metallic iron and other magnetic minerals, typical projectile materials

We assessed the hypothesis that projectile materials from the South Pole–Aitken impact event are responsible for the majority of lunar magnetic anomalies by tracking the fate of projectile materials in a suite of impact simulations. Our simulations used a three-dimensional Eulerian shock physics code with self-gravity and multiphase equations of state for crustal, mantle, and core materials (supporting online material). The rheologies of the target and projectile materials were dependent on pressure, temperature, and strain rate (28). The model Moon possessed a silicate crust 50 km thick, with a forsterite mantle and a small iron core, whereas the projectile was treated as being either homogeneous in composition or differentiated with a silicate mantle and iron core. Simulations were run for more than 1 hour after the impact, which allowed most of the ejecta to re-impact the Moon.

As a representative case, a 45° oblique impact at 15 km s^{-1} of a differentiated projectile 200 km in diameter completely excavated the crust of the Moon over an area ~1200 km in diameter and formed a thick impact melt pool in the basin interior (Fig. 3). The resulting ring of crustal thickening is similar in size to the topographic rim of the South Pole–Aitken basin, although it is not elliptical. Differences in crater shape and crustal structure between the model and observations may result from gravitational and viscous modification processes that are not accounted for in the simulations, or from the relatively low spatial resolution used to model the lunar crust. In the simulation, most of the projectile silicate mantle was vaporized and lost to space, and only ~1% of these materials were retained in the proximal ejecta. The retained projectile mantle materials were deposited downrange and exterior to the basin's excavation cavity, and possessed integrated thicknesses close to 100 m extending about one crater diameter from the basin rim. Only a negligible fraction of the projectile core was vaporized, and almost 80% of these materials were retained on the surface of the Moon. The retained projectile core materials were deposited primarily near the downrange basin rim with thicknesses up to a few kilometers.

We calculated the magnetic signature of the projectile deposits by assuming that they acquired a thermoremanence by cooling in the presence of a global dipolar field (supporting online material), although transient fields and shock remanence acquisition are also possible (8). The projectile mantle was modeled using the magnetic properties of basaltic achondrites, which have thermoremanence susceptibilities less than those of chondritic materials by about three orders of magnitude (Fig. 1). The magnetic properties of projectile core materials are not well known (29) and will depend primarily on how the projectile metal is mixed with silicate materials in the impact process (which will determine the grain sizes, shapes, and magnetostatic interactions between the metal particles). As a very conservative estimate, we used a thermoremanent susceptibility of

0.5 SI units for the core materials, which is representative of the ordinary and enstatite chondrites. Given that these chondritic materials contain only a few tens of wt% metallic iron, the true thermoremanent susceptibility of projectile core materials is probably several times our chosen value.

If the dipole field strength on the surface of the Moon was just 5 µT when this basin formed [at the low end of most paleofield estimates (5)], the projectile core materials would give rise to several magnetic anomalies with intensities of

more than 10 nT at 30 km altitude (Fig. 3). Both the intensities and the spatial distribution of these magnetic anomalies are similar to those observed adjacent to the South Pole–Aitken basin. Although most of the strong anomalies are located near the downrange rim of the impact basin, a few strong anomalies are found exterior to the basin rim as well.

We have investigated the sensitivity of these results by testing impact angles of 30°, 45°, and 60° from vertical; impact velocities of 10, 15, and 30 km s^{-1}; and impactor diameters of 150, 200,
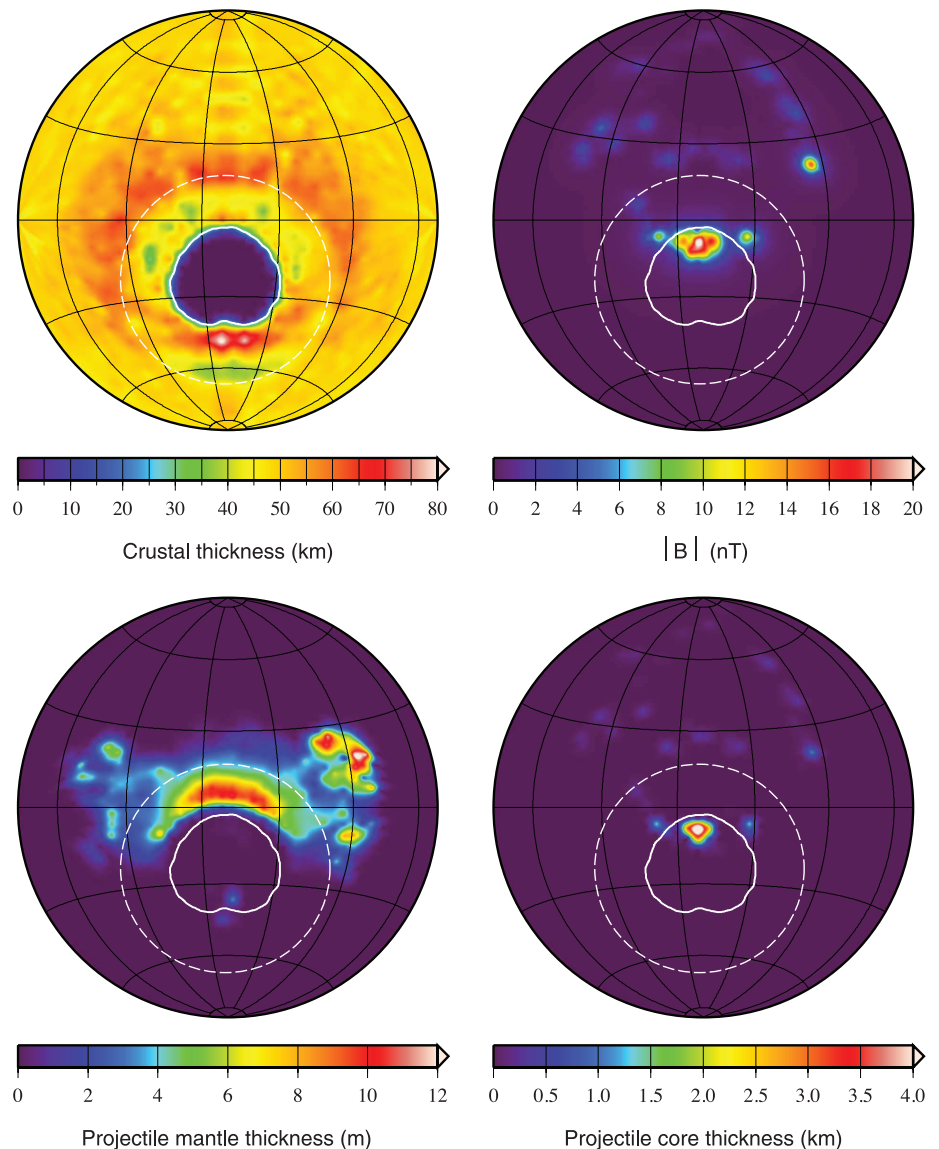

Fig. 3. Crustal thickness (top left), predicted magnetic field strength |B| (top right), integrated thickness of projectile mantle materials (bottom left), and integrated thickness of projectile core materials (bottom right) for a representative impact event sufficient to form the South Pole–Aitken basin. This oblique impact simulation used a differentiated projectile 200 km in diameter with a core 110 km in diameter. The impact direction was from south to north, the impact velocity was 15 km s^{-1}, and the impact angle from vertical was 45°. The projectile component delivered to the Moon acquired a thermoremanent magnetization in a dipolar field with a surface field strength of 5 µT. All images show half of the lunar surface and are displayed in a Lambert azimuthal equal-area projection. The solid white contour denotes where the crustal thickness has been reduced by a factor of 2 and is an approximate boundary for the extent of the deep melt sheet; the dashed outer ellipse is an approximation of the location of the final basin rim.

and 260 km (figs. S1 to S4). The overall distribution and thickness of proximal ejecta materials differed by a factor of ~3, depending on resolution, which is small in comparison to the uncertainty in the magnetic paleofield strength. For impact angles of 30° from vertical, the projectile core materials were deposited in the central portion of the basin, where they can sink through the melt sheet. For impact angles of 60° from vertical, a larger fraction of the projectile escaped the Moon's gravity, and the projectile core materials were deposited exterior to the basin rim. For homogeneous projectiles (figs. S5 to S8), the projectile materials were deposited farther downrange than for a similar impact of a differentiated projectile. If the projectile materials had the magnetic properties of average chondritic meteorites, dipole field strengths of 100 μT would generate magnetic anomalies that are similar to those observed on the Moon. Larger impact velocities favor projectile vaporization, leading to weaker magnetic anomalies. Although both differentiated and undifferentiated projectiles can account for the distribution and intensities of lunar magnetic anomalies, differentiated projectiles with impact angles of 45° most easily account for the strong anomalies that are located near the rim of the South Pole–Aitken basin. In our simulations, some projectile materials were deposited far from the basin rim, and this distal ejecta could potentially explain the existence of strong isolated anomalies on the lunar nearside, such as Reiner-γ and Descartes (Fig. 1).

Large impact events were common in the early evolution of the solar system, and these would certainly have accreted important quantities of highly magnetic materials to the crusts of all the terrestrial planets and moons. A giant

northern lowlands–forming oblique impact on Mars (30, 31) could help to explain the existence of strong crustal magnetic anomalies in the southern highlands of Mars that are otherwise difficult to understand (32, 33). Similar magnetic anomalies might be expected to surround the Caloris basin on Mercury. Impact basin–associated magnetic anomalies should scale with the amount of retained projectile materials, and hence with basin size. Being exogenic in origin, planetary magnetic anomalies could be used to search for ancient meteoritic materials.

References and Notes

1. P. Dyal, C. W. Parkin, W. D. Daily, *Rev. Geophys. Space Phys.* **12**, 568 (1974).
2. L. Hood et al., *J. Geophys. Res.* **106**, 27825 (2001).
3. D. L. Mitchell et al., *Icarus* **194**, 401 (2008).
4. M. E. Purucker, J. B. Nicholas, *J. Geophys. Res.* **115**, E12007 (2010).
5. M. Fuller, S. M. Cisowski, in *Geomagnetism*, J. A. Jacobs, Ed. (Academic Press, London, 1987), vol. 2, pp. 307–455.
6. J. Gattacceca et al., *Earth Planet. Sci. Lett.* **299**, 42 (2010).
7. W. D. Daily, P. Dyal, *Phys. Earth Planet. Inter.* **20**, 255 (1979).
8. L. L. Hood, Z. Huang, *J. Geophys. Res.* **96**, 9837 (1991).
9. D. Crawford, P. Schultz, *Int. J. Impact Eng.* **23**, 169 (1999).
10. D. R. Stegman, A. M. Jellinek, S. A. Zatman, J. R. Baumgardner, M. A. Richards, *Nature* **421**, 143 (2003).
11. M. A. Wieczorek et al., *Rev. Mineral. Geochem.* **60**, 221 (2006).
12. M. Le Bars, M. A. Wieczorek, Ö. Karatekin, D. Cébron, M. Laneuville, *Nature* **479**, 215 (2011).
13. C. A. Dwyer, D. J. Stevenson, F. Nimmo, *Nature* **479**, 212 (2011).
14. L. Hood, *Icarus* **211**, 1109 (2011).
15. J. Halekas, R. Lin, D. Mitchell, *Meteorit. Planet. Sci.* **38**, 565 (2003).
16. J. Halekas et al., *J. Geophys. Res.* **106**, 27841 (2001).
17. L. Hood, N. Artemieva, *Icarus* **193**, 485 (2008).
18. D. Wang, R. Van der Voo, D. R. Peacor, *Geosphere* **1**, 138 (2005).
19. P. Rochette, J. Gattacceca, A. V. Ivanov, M. A. Nazarov, N. S. Bezaeva, *Earth Planet. Sci. Lett.* **292**, 383 (2010).
20. I. Garrick-Bethell, B. P. Weiss, D. L. Shuster, J. Buz, *Science* **323**, 356 (2009).
21. E. K. Shea et al., *Science* **335**, 453 (2012).
22. R. L. Korotev, *J. Geophys. Res.* **105**, 4317 (2000).
23. I. Garrick-Bethell, M. T. Zuber, *Icarus* **204**, 399 (2009).
24. R. Tagle, L. Hecht, *Meteorit. Planet. Sci.* **41**, 1721 (2006).
25. R. Tagle, R. T. Schmitt, J. Erzinger, *Geochim. Cosmochim. Acta* **73**, 4891 (2009).
26. R. L. Korotev, *J. Geophys. Res.* **92**, E491 (1987).
27. E. Pierazzo, H. J. Melosh, *Meteorit. Planet. Sci.* **35**, 117 (2000).
28. L. E. Senft, S. Stewart, *Earth Planet. Sci. Lett.* **287**, 471 (2009).
29. A. Brecher, L. Albright, *J. Geomag. Geoelectr.* **29**, 379 (1977).
30. J. C. Andrews-Hanna, M. T. Zuber, W. B. Banerdt, *Nature* **453**, 1212 (2008).
31. M. M. Marinova, O. Aharonson, E. Asphaug, *Nature* **453**, 1216 (2008).
32. J. E. P. Connerney et al., *Geophys. Res. Lett.* **28**, 4015 (2001).
33. D. J. Dunlop, J. Arkani-Hamed, *J. Geophys. Res.* **110**, E12S04 (2005).
34. D. E. Smith et al., *Geophys. Res. Lett.* **37**, L18204 (2010).

Reconstruction of *Microraptor* and the Evolution of Iridescent Plumage

Quanguo Li,[1] Ke-Qin Gao,[2] Qingjin Meng,[1] Julia A. Clarke,[3] Matthew D. Shawkey,[4]* Liliana D'Alba,[4] Rui Pei,[5] Mick Ellison,[5] Mark A. Norell,[5] Jakob Vinther[3,6]

Iridescent feather colors involved in displays of many extant birds are produced by nanoscale arrays of melanin-containing organelles (melanosomes). Data relevant to the evolution of these colors and the properties of melanosomes involved in their generation have been limited. A data set sampling variables of extant avian melanosomes reveals that those forming most iridescent arrays are distinctly narrow. Quantitative comparison of these data with melanosome imprints densely sampled from a previously unknown specimen of the Early Cretaceous feathered *Microraptor* predicts that its plumage was predominantly iridescent. The capacity for simple iridescent arrays is thus minimally inferred in paravian dinosaurs. This finding and estimation of *Microraptor* feathering consistent with an ornamental function for the tail suggest a centrality for signaling in early evolution of plumage and feather color.

Feather colors in extant birds (Aves) are generated from pigments and a variety of nanostructural architectures (1, 2). Iridescent colors, an integral part of the avian plumage color gamut involved in signaling and display, are produced through coherent light scattering by laminar or crystal-like arrays generated by layers of materials with different refractive indices—namely, keratin, melanin, and sometimes air—in feather barbules (1, 2). Melanosomes can be arranged in single or multiple layers (1, 2), and recent work shows that even slight organization of melanosomes can produce weakly iridescent (glossy) colors (3). Iridescent nanostructures are diverse and have evolved independently numerous times in extant birds (4), but whether they are exclusively avian innovations or appear earlier in dinosaur evolution has been unknown.

Thus far, fossil evidence of iridescent plumage has been limited to a 47-million-year-old isolated avian feather from Germany (Grube Messel) (5). This feather preserved in fine nanostructural detail the organization typical of many iridescent avian melanosome arrays. Such pristine preservation is rare, however, and so far unknown in

[1]Beijing Museum of Natural History, 126 Tianqiao South Street, Beijing 100050, People's Republic of China. [2]School of Earth and Space Sciences, Peking University, Beijing 100871, People's Republic of China. [3]Department of Geological Sciences, University of Texas at Austin, 1 University Station C1100, Austin, TX 78712, USA. [4]Department of Biology and Integrated Bioscience Program, University of Akron, Akron, OH 44325–3908, USA. [5]Department of Paleontology, American Museum of Natural History, 79th Street at Central Park West, New York, NY 10024, USA. [6]Department of Geology and Geophysics, Yale University, New Haven, CT 06520–8109, USA.

*To whom correspondence should be addressed. E-mail: shawkey@uakron.edu

Supporting Online Material for

An Impactor Origin for Lunar Magnetic Anomalies

Mark A. Wieczorek,* Benjamin P. Weiss, Sarah T. Stewart

*To whom correspondence should be addressed. E-mail: wieczor@ipgp.fr

This PDF file includes:

SOM Text

Figs. S1 to S8

Tables S1 to S4

References

1 Thermoremanence susceptibility of lunar and meteoritic materials

The thermoremanent magnetization acquired by most rocks is approximately proportional to the magnetizing field for field strengths less than about 50-100 μT (*35–37*). This can be expressed by the relation

$$\mathbf{M}_{tr} = \chi_{TRM}\,\mathbf{H},\tag{1}$$

where M_{tr} is the thermoremanent magnetization (in units of A m^{-1}), χ_{TRM} is the thermoremanence susceptibility (sometimes denoted by the symbol c (*38*), in SI units), and H is the magnetizing field (in units of A m^{-1}). Experiments show (*39–41*) that the ratio of thermoremnent magnetization to saturation remanent magnetization, M_{rs}, is related linearly to the applied magnetic field B (in units of T)

$$B = a\,M_{tr}/M_{rs}.\tag{2}$$

The proportionality constant a varies by a factor of about 3 to 5 for a wide range of geologic materials, and is about 3×10^{-3} for typical equant grains of multidomain iron (*40*). Using the relation $B = \mu_0 H$, the thermoremanence susceptibility can be expressed as

$$\chi_{TRM} = \mu_0\,M_{rs}/a,\tag{3}$$

where μ_0 is the magnetic constant, $4\pi \times 10^{-7}$ T m A^{-1}.

We gathered measurements of the saturation remnant magnetization per unit mass m_{rs} (in units of A m^2 kg^{-1}; equivalently M_{rs}/ρ, where ρ the sample density) acquired over the last four decades for lunar samples with relatively well-characterized lithologies (Table S1). These include unbrecciated mare basalts, pristine highlands rocks (defined as unbrecciated or monomict anorthosites and Mg-suite rocks uncontaminated by meteoritic materials), and mafic impact melt breccias (as defined by ref. (*22*)). Other highlands breccias (e.g., granulitic breccias) typically are less well-defined petrographically but have similar quantities of ferromagnetic minerals as the mafic impact melt breccias (*5*). The lunar soils and regolith breccias are not considered because the regolith is extremely thin (<15 m (*42*)) and would not

2

be unidirectionally magnetized given the continuous process of impact gardening. The average magnetic properties of lunar materials are presented in Table S2 under the assumption that the m_{rs} measurements are log-normally distributed. The average magnetic properties of chondritic and achondritic meteorites are given in Table S3.

2 Magnetic field of material magnetized by a central dipole

The Gauss coefficients corresponding to a volume of material magnetized by a now extinct central dipolar field were derived by ref. (*43*). The magnetization in this derivation was confined to lie between an upper surface $r(\theta, \phi)$, where θ and ϕ are respectively colatitude and longitude, and a lower spherical surface with (arbitrary) radius R. The amplitude of the relief r relative to the average value was assumed to be small. The ratio between the acquired thermoremanent magnetization $\mathbf{M}$ and magnetizing field $\mathbf{H}$ was assumed to be linear and equal to χ_{TRM}, and the magnetizing dipolar field was assumed to be aligned with the z axis with a dipole moment p.

Using complex orthonormalized spherical harmonics, Y_l^m, that employ the Condon-Shortley phase of $(-1)^m$ (*44*), the radius of the upper surface was expanded as

$$r(\theta, \phi) = \sum_{l=0}^{L} \sum_{m=-l}^{l} r_l^m Y_l^m(\theta, \phi),$$ (4)

where l is the spherical harmonic degree, m is the spherical harmonic order, and L is the maximum degree of the expansion. We note that a typographic error is present in their derivation as the average radius of r (here defined to be a) was set equal to r_0^0 instead of $r_0^0/\sqrt{4\pi}$, which is required for the employed spherical harmonic normalization. Nevertheless, ref. (*43*) arrived at the correct results in their discussion, despite this inconsistency. (It is only necessary to replace r_{00} in their manuscript by the average radius of the function r.) The correct equation for the Gauss coefficients, after taking into

account an additional selection rule not used by ref. (*43*), is

$$
g_l^m = \frac{c\,p\,\mu_0}{4\,\pi\,a^3} \sum_{l'=l-1,l+1} \frac{r_{l'}^m}{a} \sqrt{\frac{2l'+1}{(2l+1)^3}}\, C_{10l'0}^{l0}
$$
$$
\times \left[(2l-2-m)\, C_{10l'm}^{lm} - \sqrt{2}\sqrt{l'(l'+1)-m(m+1)}\, C_{1,-1,l',m+1}^{lm} \right],
\tag{5}
$$

where the sum over l' is understood to be only for the two listed values. The relation between Schmidt semi-normalized, g_{lm}, and the above complex normalized coefficients is

$$
g_{lm} = \sqrt{\frac{2l+1}{4\pi}} \begin{cases} g_l^0 & m=0 \\ (-1)^m\,\sqrt{2}\;\text{Real}\,(g_l^m) & m>0 \\ (-1)^{m+1}\,\sqrt{2}\;\text{Imag}\left(g_l^{|m|}\right) & m<0. \end{cases}
\tag{6}
$$

The magnetic potential is given by the expression

$$
U(\mathbf{r}) = a \sum_{l=1}^{L} \sum_{m=-l}^{l} \left(\frac{a}{r}\right)^{l+1} g_{lm}\, Y_{lm}(\theta,\phi),
\tag{7}
$$

where the spherical harmonic functions Y_{lm} are Schmidt semi-normalized, and the magnetic field $\mathbf{B}$ is equal to the gradient of the potential

$$
\mathbf{B}(\mathbf{r}) = -\nabla U(\mathbf{r}).
\tag{8}
$$

For computational purposes, we note that the Wigner 3-j symbols are related to the Clebsch-Gordan coefficients by (*44, p. 236*)

$$
C_{l_1 m_1 l_2 m_2}^{lm} = (-1)^{l_1-l_2+m}\sqrt{2l+1} \begin{pmatrix} l_1 & l_2 & l \\ m_1 & m_2 & -m \end{pmatrix}.
\tag{9}
$$

3   Impact simulation methods

The formation of impact basins approximately the size of South Pole-Aitken was modeled using the CTH shock physics code (*45*) in three dimensions with self-gravity (*46*). The Moon was initialized in gravitational equilibrium with an estimate for the $0.5\,\text{Gyr}$ thermal profile (*47*), and given the early time of the South Pole-Aitken impact, molten cores were assumed for both the projectile and Moon. Multiphase model equations of state were used for molten iron (*48*), forsterite (2008 update by Melosh based on

ref. (*49*)), and silica (*50*) to represent core, mantle, and crustal materials, respectively. The simulations utilized the adaptive mesh refinement feature in CTH. Since the simulations were performed in Cartesian geometry, for visualization purposes, the thickness of crustal and projectile materials were determined by projecting and summing the mass of these materials onto an approximately 130 km by 130 km equal area grid at the surface.

The projectile had a resolution of 5 or 10 km until the shock wave was fully released. The crust and upper mantle resolution was typically 20 km in the impacted hemisphere, and sensitivity tests were run with resolutions of 10 to 40 km. Though these resolutions were sufficient to quantify the size of the region were the crust was entirely excavated and the general redistribution of the crust, these resolutions (in combination with the coarse grid used for visualization) are probably too low to quantify the fine details of the post-impact stratigraphy. The overall distribution and thickness of proximal ejecta materials, which is the main purpose of this study, was found to be qualitatively similar in these resolution tests, with differences of a factor of about three (Figs. S1 and S5). It is emphasized that this factor of three is small in comparison to the uncertainty in the strength of the field that magnetized these deposits, which is estimated to be between about 1 to 120 μT (*5, 20*). In Figs. S1-S8, the mottled appearance of the crustal thickness on the opposite hemisphere of the impact basin is an artifact due to a lower resolution of the crust in this region. Vaporized and finely dispersed materials are removed from the calculation for computational expediency using a density criteria (typically 0.1 kg m^{-3}).

The pressure, temperature, and strain-rate dependent rheological model was an updated version of ref. (*28*). In this work, the dynamic weakening criteria includes the effect of overburden pressure (*51,52*). The lunar crust was modeled with the parameters for granite in ref. (*28*). For the mantle, the limiting yield surface was defined by dislocation creep for olivine based on laboratory experiments (*53*). The peridotite solidus and olivine liquidus were used to calculate melting in the mantle (*54*), which was implemented in a similar manner as in ref. (*55*). Iron was assumed to be hydrodynamic.

The sizes of the excavation cavity and the final basin diameter were not significantly affected by these

updates to the rheological model used in ref. (*28*). One change affects our investigation of the distribution of materials near the basin rim. In previous numerical simulations of impact cratering, materials heated to and above the solidus were essentially modeled as hydrodynamic fluids. It has long been recognized that the depth of shock-induced melting exceeds the excavation depth in basin-forming events (*56*). Thus, in such large impacts, the collapse of the transient cavity involves significant amounts of melted material. As a result, the gravitationally-driven collapse of the transient crater led to overshoot and sloshing of mantle materials onto the surrounding crust (*55*); however, widespread surface deposits of mantle materials are not observed around South Pole-Aitken basin.

In this work, it is recognized that the collapse of the mantle involves a two-phase flow of melt and solid clasts. Under the high strain rates of crater collapse, the ratio of clast inertia to viscous forces (the Bagnold number) is high; as a result, the shear stresses are determined by collisions between the solid clasts (*57*). Furthermore, the convergent geometry ensures a high volume fraction of clasts mixing into the melt. Here, this complex debris flow of mantle materials was modeled using a simplified approach: when the temperature exceeded the solidus, a pressure-dependent friction law (coefficient of 0.1 to 0.2 based on melt-lubricated faults (*58*)) was used at high strain rates ($>10^{-4}$ s^{-1}), and a Newtonian fluid rheology was used at low strain rates when the viscosity of the fluid dominates (*59*).

During collapse of the transient cavity, the frictional strength of the melt-clast mixture inhibits significant overshoot of mantle material. As a result, most of the deposits near the basin rim are primary ejecta from the excavation cavity. In the three-dimensional simulations, the basin structure about an hour after the impact has two major features: (i) an inner region filled with a mixture of melt and solid clasts and bounded by the cold crust folded over at the rim of the excavation cavity, and (ii) a terrace of thinned and translated cold crust surrounded by the original crust thickened by ejecta deposits. We identify the boundary between the thinned terrace and thickened crust as the approximate final basin diameter, which is analogous to the outer ellipse in Fig. 1. The thickest crust in our simulations is located in the down-range direction, consistent with the thickened crust north of the South Pole-Aitken basin as derived from

gravity and topography data (*11*) (though see (*60*) for a non-impact explanation for this thickened crust).

Most of the crust in the inner region, denoted by white lines in Figs. 3 and S1 to S8, was excavated during formation of the transient cavity; some crustal materials remain trapped beneath the projectile and are melted and partially vaporized by the impact shock. The deep thermal anomaly from the impact has a diameter slightly larger than the region of excavated crust. We hypothesize that this melt pool fractionally crystallizes (*61*), possibly incorporating portions of the adjacent crust, to form a new, thinner crust in the inner basin. This secondary crust would correspond to the mafic geochemical anomaly associated with the interior of the South Pole-Aitken basin, approximated by the inner solid white line in Fig. 1. In all cases studied here, the basin is approximately circular. However, the hot inner region is offset downrange from center, and post-impact modification may affect the final shape. In addition, the calculated distributions of crust and projectile materials in and near the hot inner region is likely to be modified during post-impact processes.

We considered impact velocities from 5 to 30 km s^{-1}, impact angles of 30, 45 and 60 degrees, bolide radii from 75 to 260 km, and homogeneous bolides and differentiated bolides with 1/3 core mass fraction. The probability distribution of impact parameters is centered around 45° and 15 km s^{-1} (*62*), where a differentiated projectile 200 km in diameter forms an approximately 2000 km diameter basin. The peak shock pressures were about 120, 250, and 1000 GPa for impact velocities of 10, 15, and 30 km s^{-1}, respectively. The 30 km s^{-1} events led to significant amounts of vaporization of the silicates in the projectile (*63*) and the ejecta deposits lack significant concentrations of the silicate component of the projectile. Much of the vapor escapes the Moon's gravity or is finely dispersed over the lunar surface. Below about 10 km s^{-1}, vaporization is negligible. For the distribution of probable impact velocities, iron in the projectile core undergoes minor amounts of shock-induced vaporization. In 60° events, most of the iron core in differentiated projectiles is jetted from the growing transient cavity at velocities exceeding the escape velocity of the Moon. The amounts of projectile mantle and core retained on the surface of the Moon for all our simulations (excluding the vaporized component that was discarded) are summarized

7

in Table S4.

During the impact event, the projectile deformed and lined the transient cavity floor, and the vaporized mass fraction escaped on non-ballistic trajectories. The melted and solid portions of the projectile mixed with the lunar crust at the bottom of the transient cavity, and the multi-material code advected the mixed materials together through the mesh. The ballistic ejecta is composed primarily of excavated lunar crust. Figs. S1-S8 present the crustal thickness and integrated thickness of projectile materials mixed into the crust for a selection of simulation runs. The transient cavity formation time was about 500 s, and the basin formation time (including deposition of the continuous ejecta blanket) was about 1 hour. The simulations were run typically for more than one hour, with some cases up to 4 hours to examine far-field ejecta. Some of the high velocity ejecta passed beyond the spatial confines of the simulation domain and were removed from consideration. The deposition of ejecta on the opposite hemisphere of the Moon would be affected by the Moon's rotation (*64*), which is not accounted for in our simulations.
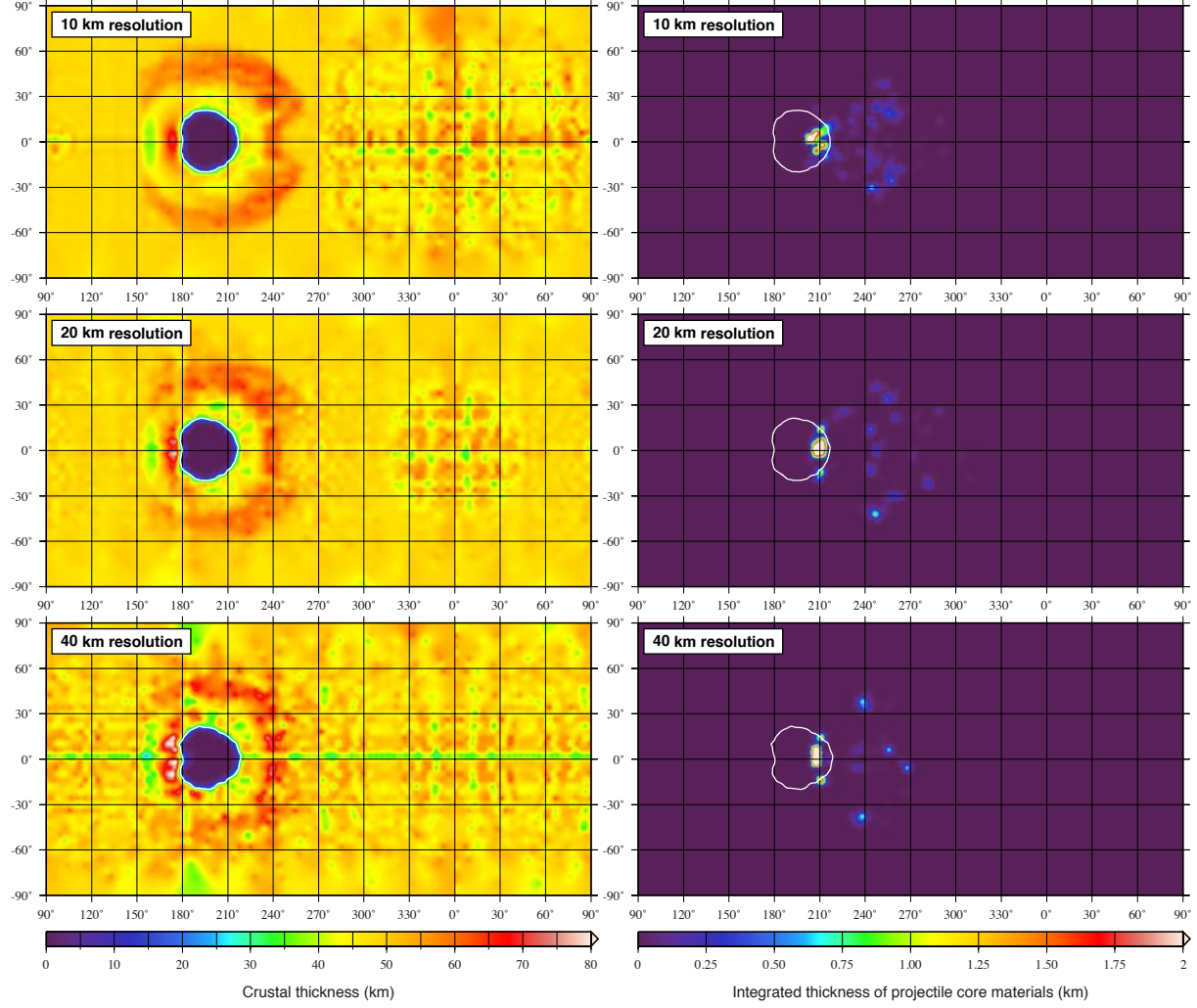
Fig. S1. Comparison of simulation results with different spatial resolutions of the lunar crust. Crustal thickness (left) and integrated thickness of projectile core materials (right) are shown for simulations with 10-km (top), 20-km (middle), and 40-km (bottom) resolutions in the crust of the impacted hemisphere. For these oblique impact simulations, the impact direction was from left to right, the impact velocity was 15 km s^{-1}, the impact angle from vertical was 45°, and the projectile was differentiated with a 100 km radius and a 55 km radius core. The map projection is simple cylindrical, and the solid white contour denotes where the crustal thickness has been reduced by a factor of two. The maximum integrated thickness of core materials is 5.4, 4.1, and 5.6 km for the 10, 20, and 40 km resolution simulations, respectively. Results for these tests are shown 55 minutes following the impact.
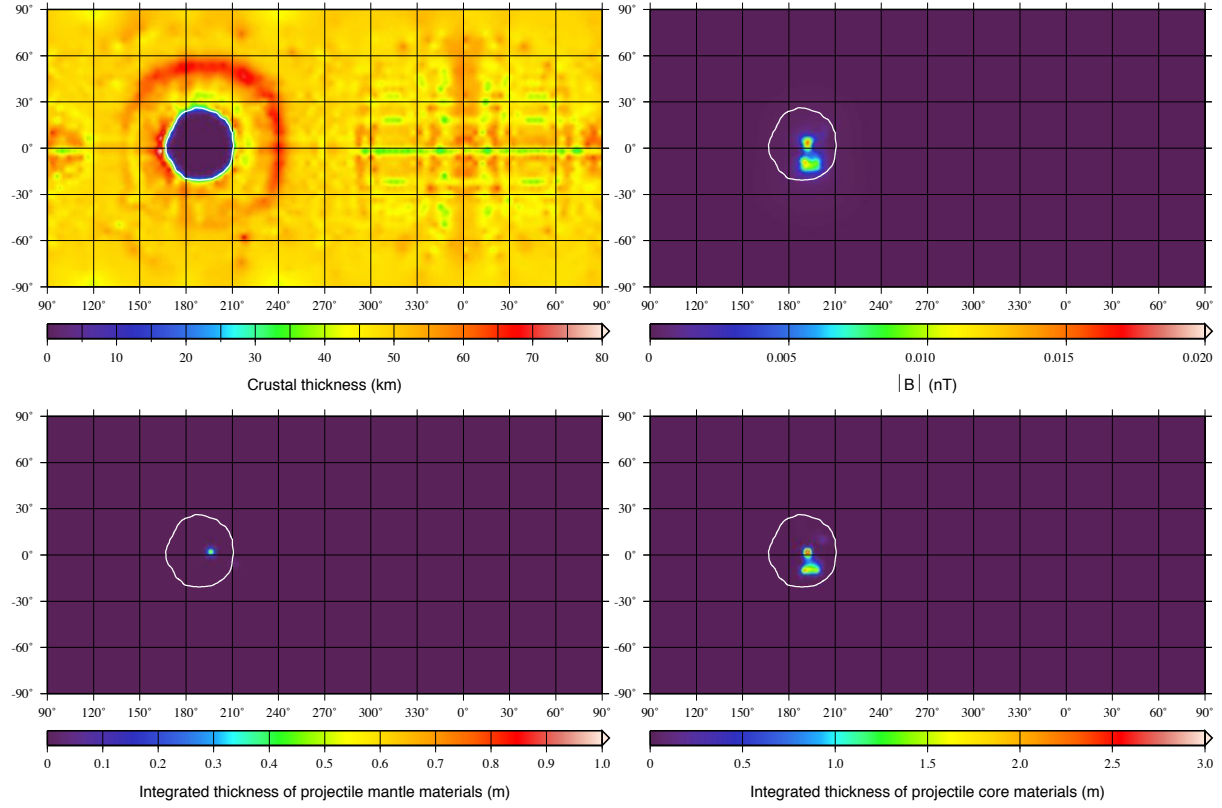
Fig. S2A. Crustal thickness (top left), integrated projectile mantle thickness (bottom left), integrated projectile core thickness (bottom right), and predicted magnetic field strength (top right) for a representative South Pole-Aitken basin forming impact event. For this oblique impact simulation, the impact direction was from left to right, the impact velocity was 30 km s^{-1}, the impact angle from vertical was 30°, and the 75 km radius projectile was differentiated with a 41 km radius core. The projectile mantle component delivered to the Moon was assumed to possess the thermoremanence susceptibility of eucrite meteorites (6.59×10^{-4} SI units), whereas the projectile core materials were assumed to possess a thermoremanence susceptibility of 0.5 SI units, which is representative of ordinary and enstatite chondrites. The magnetic field strength was determined by assuming the projectile materials acquired a thermoremanent magnetization in a dipolar field with a surface field strength of 5 μT. The map projection is simple cylindrical, and the solid white contour denotes where the crustal thickness has been reduced by a factor of two. The simulations had a resolution in the crust of 20 km on the impacted hemisphere, and the results are shown 67 minutes following the impact.
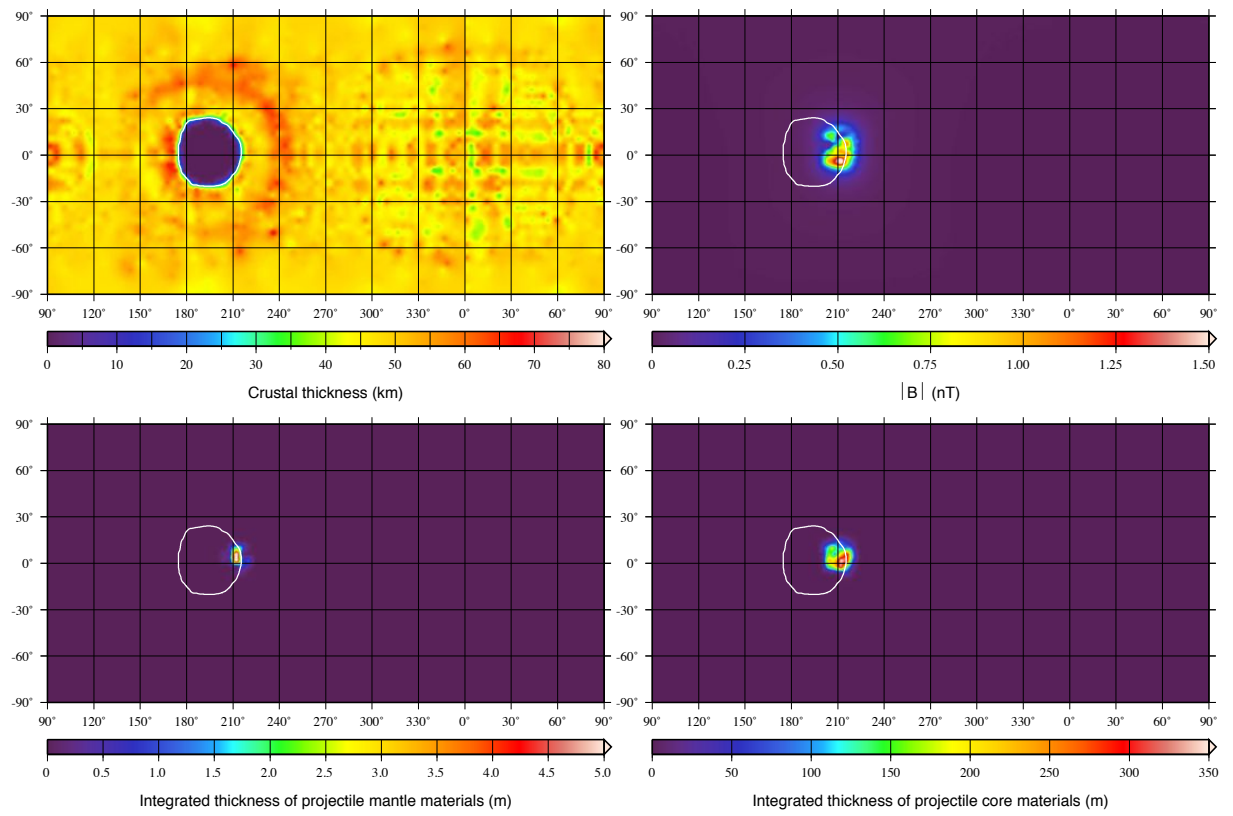
10

Fig. S2B. Same as Fig. S2A, but for an impact angle of 45° from vertical.
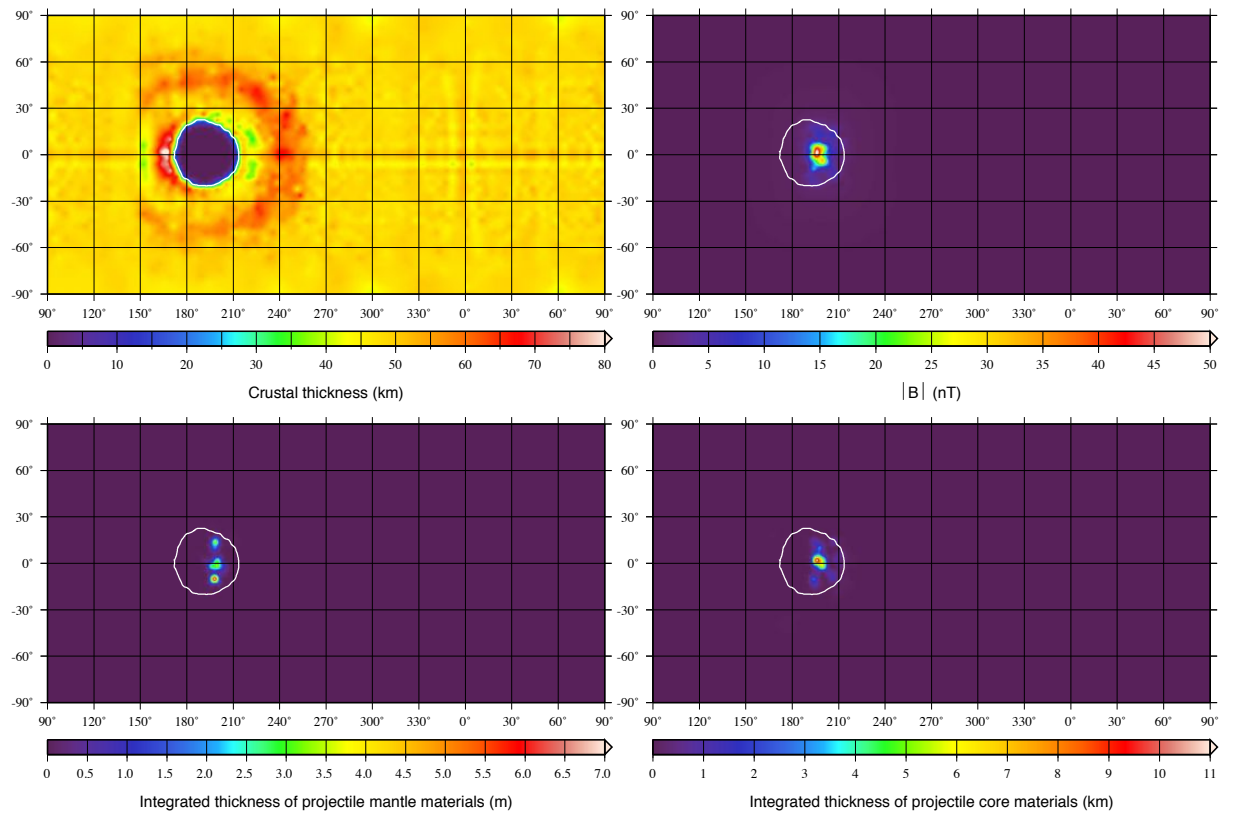
11

Fig. S3A. Impact of a 100 radius differentiated projectile with a 55 km radius core, an impact velocity of 15 km s^{-1}, and an impact angle of 30° from vertical. Format and other parameters the same as in Fig. S2A.
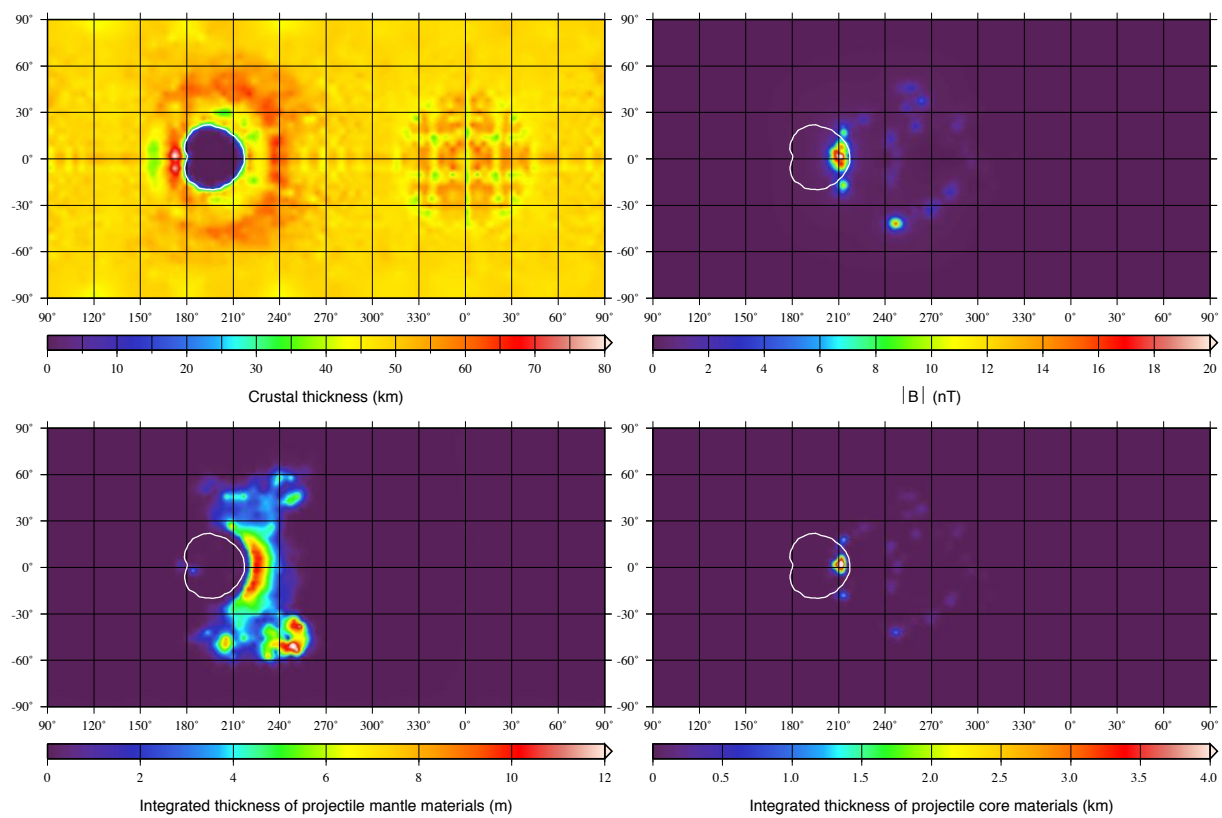
Fig. S3B. Same as Fig. S3A, but for an impact angle of 45° from vertical.

13

Fig. S3C. Same as Fig. S3A, but for an impact angle of 60° from vertical.
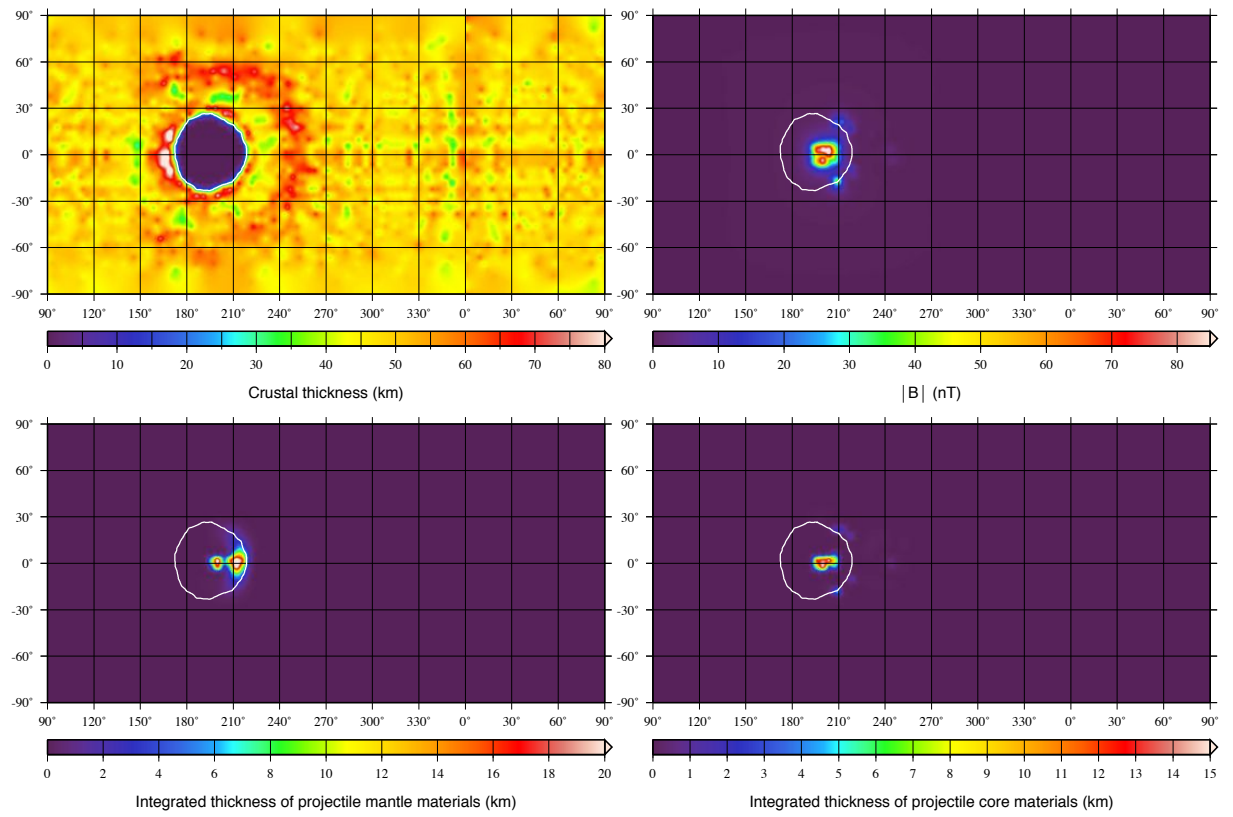
Fig. S4A. Impact of a 130 km radius differentiated projectile with a 71 km radius core, an impact velocity of 10 km s^{-1}, an impact angle of 30° from vertical, and a simulation resolution in the crust of 40 km. Format and other parameters the same as in Fig. S2A.

15

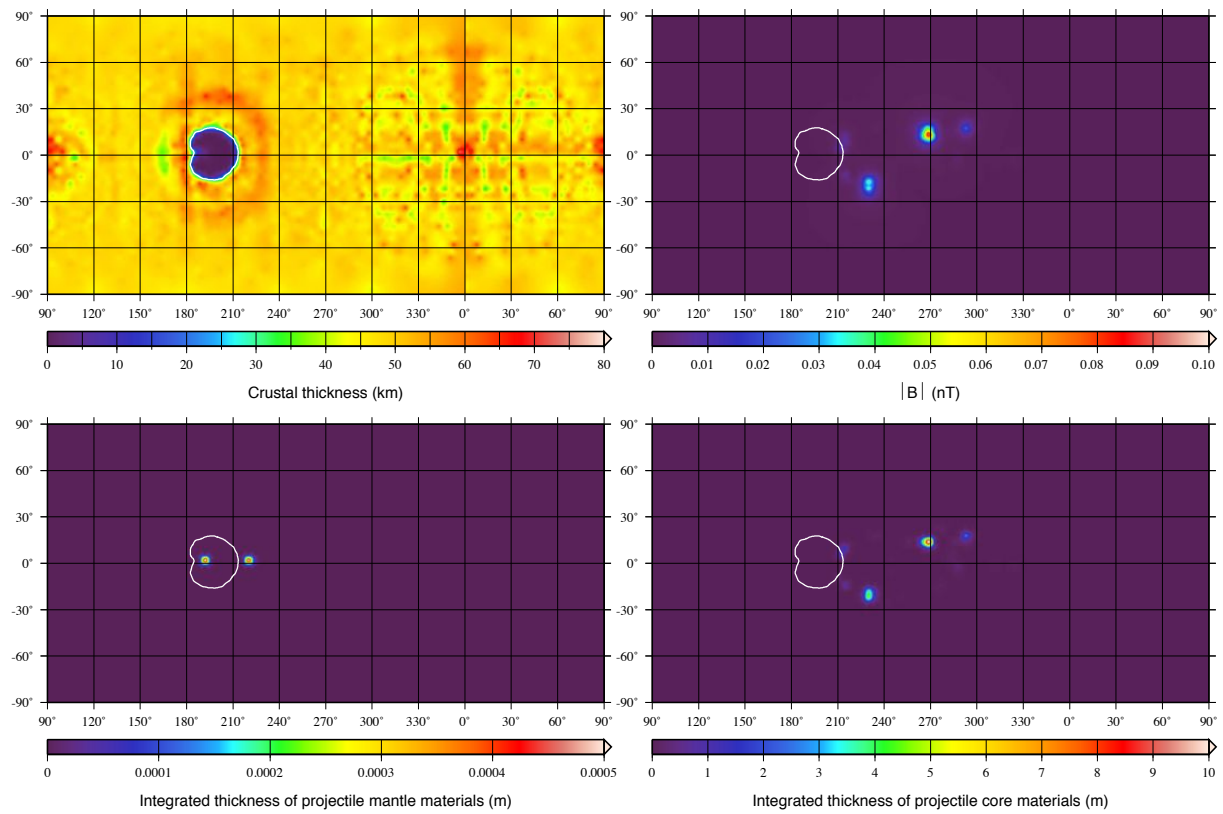**Fig. S4B.** Same as Fig. S4A, but for an impact angle of 45° from vertical, and a simulation resolution in the crust of 20 km.

Fig. S4C. Same as Fig. S4A, but for an impact angle of 60° from vertical, and a simulation resolution in the crust of 20 km.
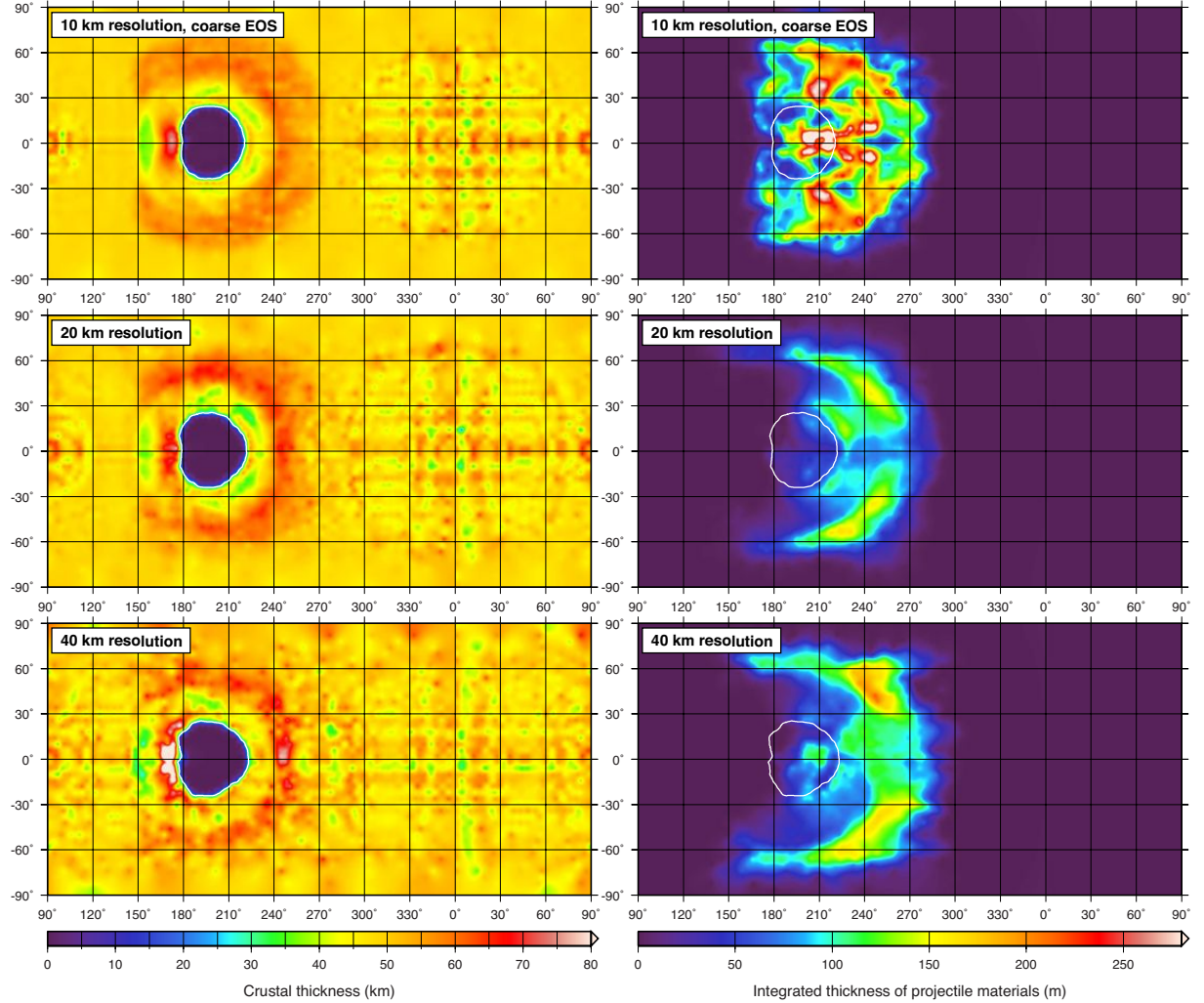
Fig. S5. Comparison of simulation results with different resolutions of the lunar crust and different resolution tabulations of the equation of state. Crustal thickness (left) and integrated thickness of projectile materials (right) 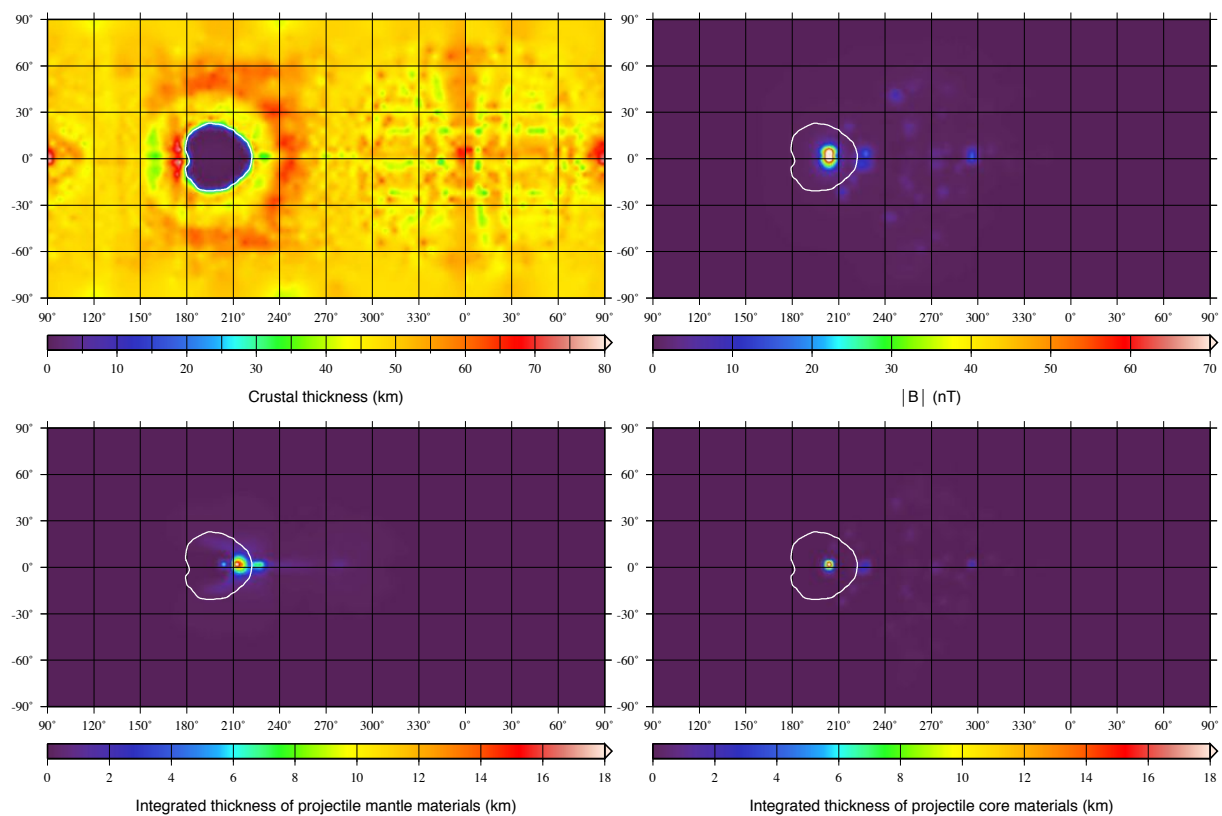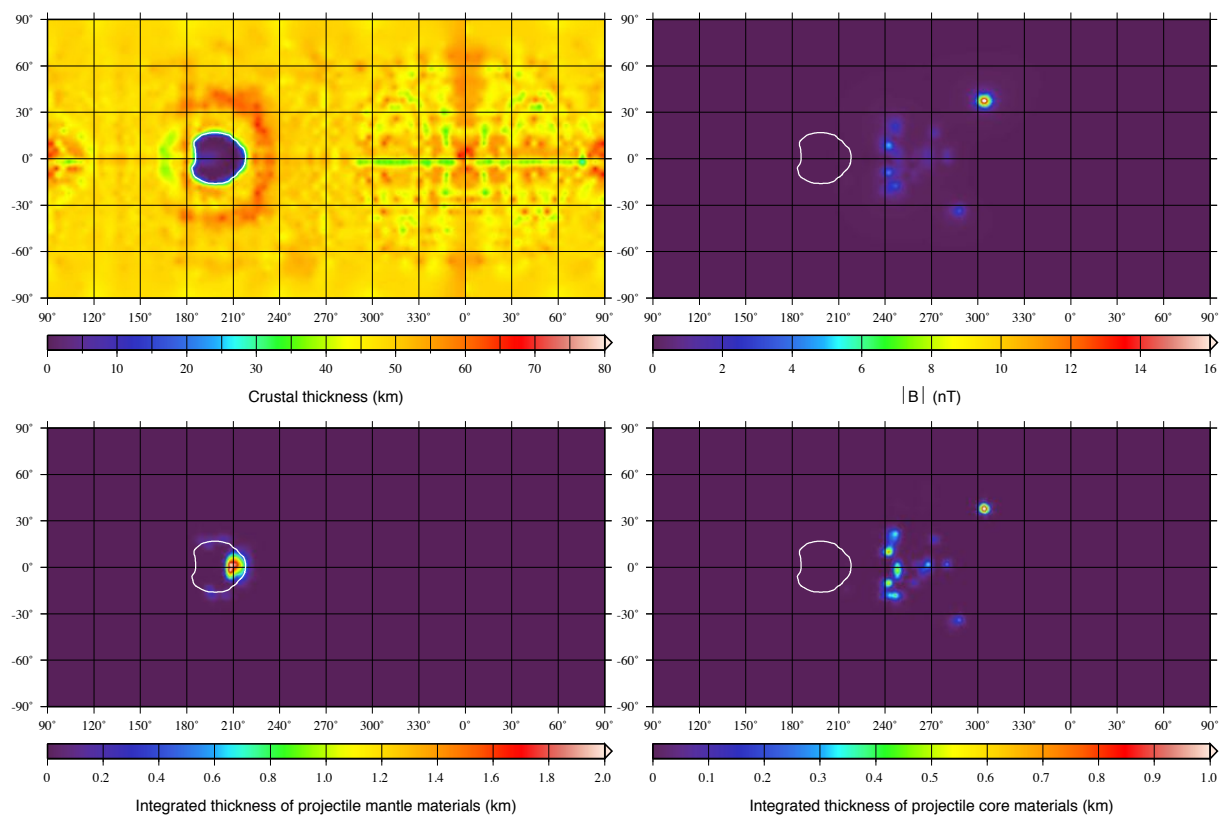are shown for simulations with 10-km (top), 20-km (middle), and 40-km (bottom) resolutions in the crust on the impacted hemisphere. For these oblique impact simulations, the impact direction was from left to right, the impact velocity was 15 km s^{-1}, the impact angle from vertical was 45°, and the projectile was homogeneous in material properties with a 125 km radius. The map projection is simple cylindrical, and the solid white contour denotes where the crustal thickness has been reduced by a factor of two. The 10-km case used a more coarsely gridded equation of state table than the other two simulations. The maximum integrated thicknesses of projectile materials are 437, 171, and 217 km, which are shown 66 minutes following the impact, for the 10, 20, and 40 km resolution simulations, respectively.

18
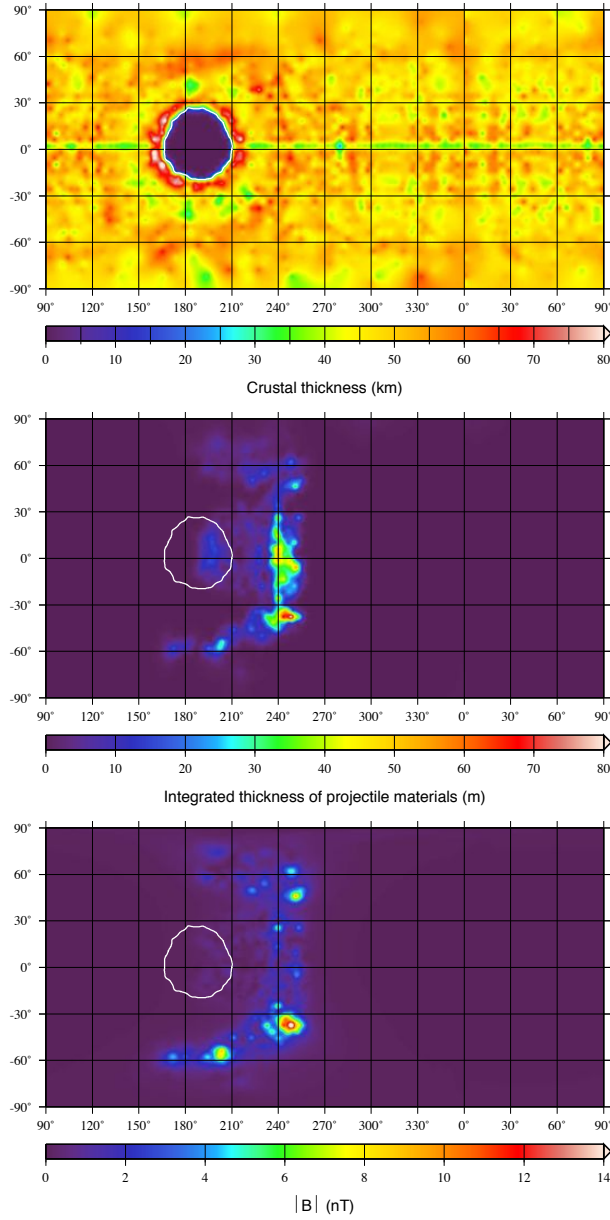
Fig. S6A. Crustal thickness (top), integrated projectile thickness (middle), and predicted magnetic field strength (bottom) for a representative South Pole-Aitken basin forming impact event. For this oblique impact simulation, the impact direction was from left to right, the impact velocity was 30 km s^{-1}, the impact angle from vertical was 30°, and the projectile was homogeneous with a 79 km radius. The simulation resolution in the crust was 40 km. The projectile component delivered to the Moon was assumed to possess the average thermoremanence susceptibility of chondritic meteorites (0.453 SI units), and the magnetic field strength was determined by assuming the projectile materials acquired a thermoremanent magnetization in a dipolar field with a surface field strength of 100 μT. The map projection is simple cylindrical, and the solid white contour denotes where the crustal thickness has been reduced by a factor of two. The simulation results are shown 83 minutes following the impact.
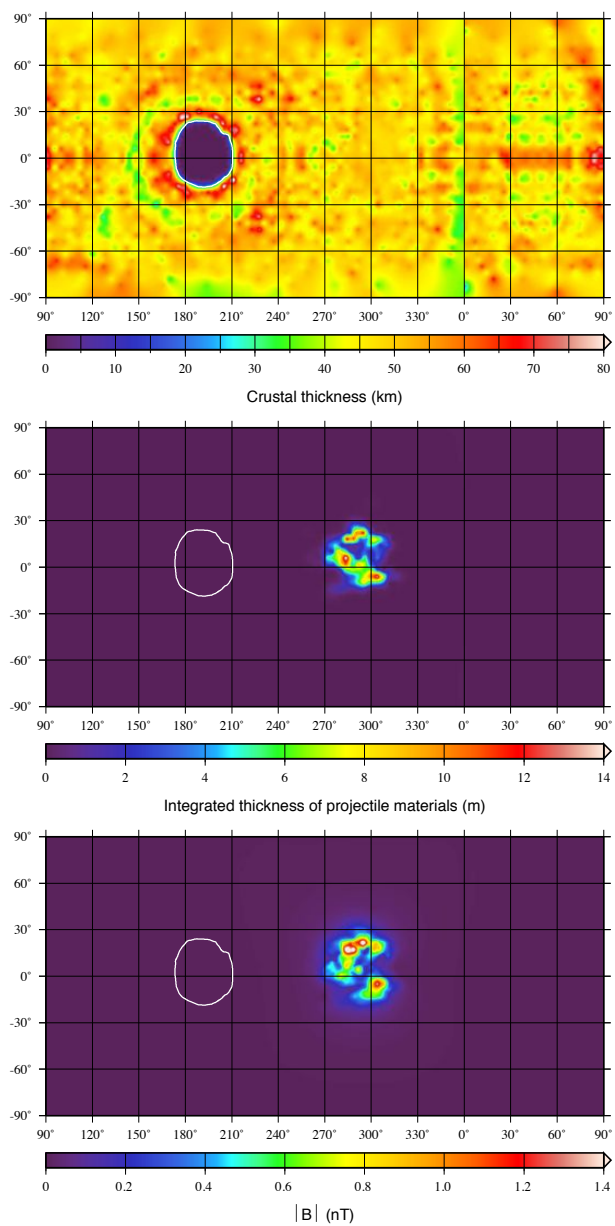
Fig. S6B. Same as Fig. S6B, but for an impact angle of 45° from vertical, and 2.8 hours following the impact.
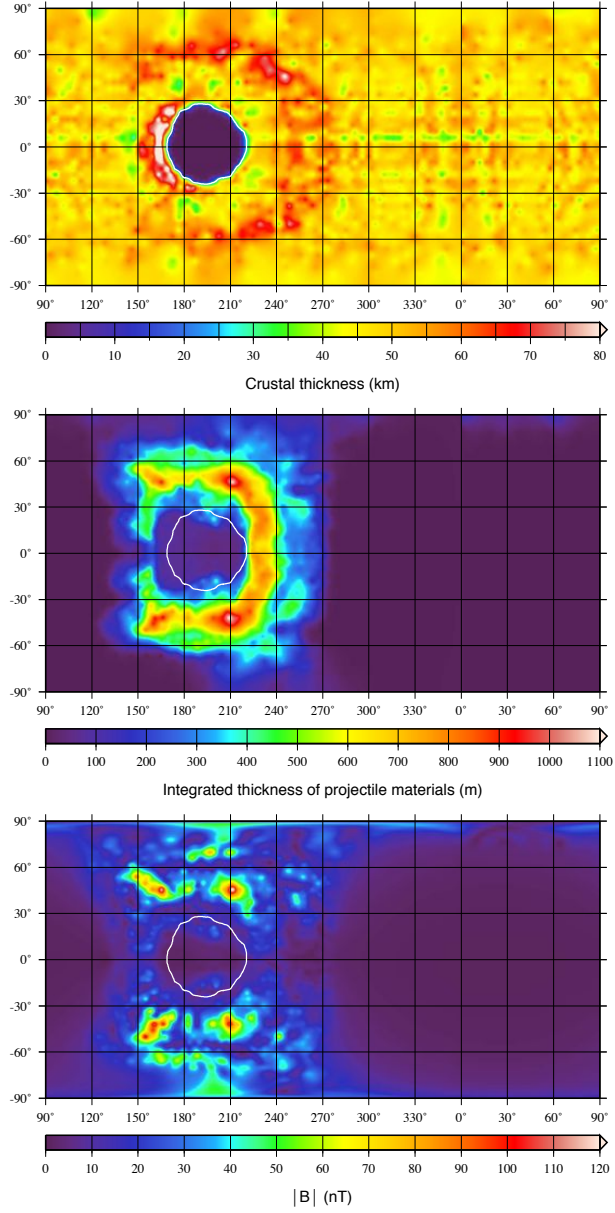
Fig. S7A. Impact of a 125 km radius homogeneous projectile at an impact velocity of 15 km s^{-1} and an impact angle of 30° from vertical. Results are shown 67 minutes following the impact. Format and other parameters the same as in Fig. S6A.

Fig. S7B. Same as Fig. S7A, but for an impact angle of 45° from vertical, a simulation resolution in the crust of 10 km, and 67 minutes following the impact.

Fig. S7C. Same as Fig. S7A, but for an impact angle of 60° from vertical, and 67 minutes following the impact.
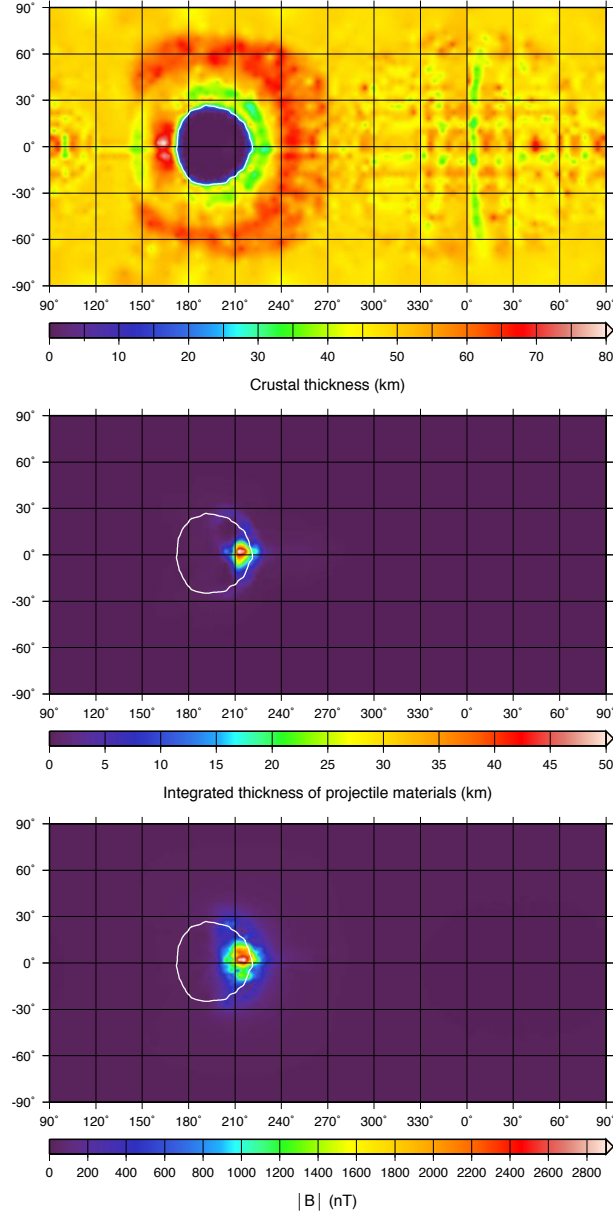
Fig. S8A. Impact of a 150 km radius homogeneous projectile at an impact velocity of 10 km s^{-1} and an impact angle of 30° from vertical. Results are shown 65 minutes following the impact, and the crustal resolution is 20 km. Format and other parameters the same as in Fig. S6A.
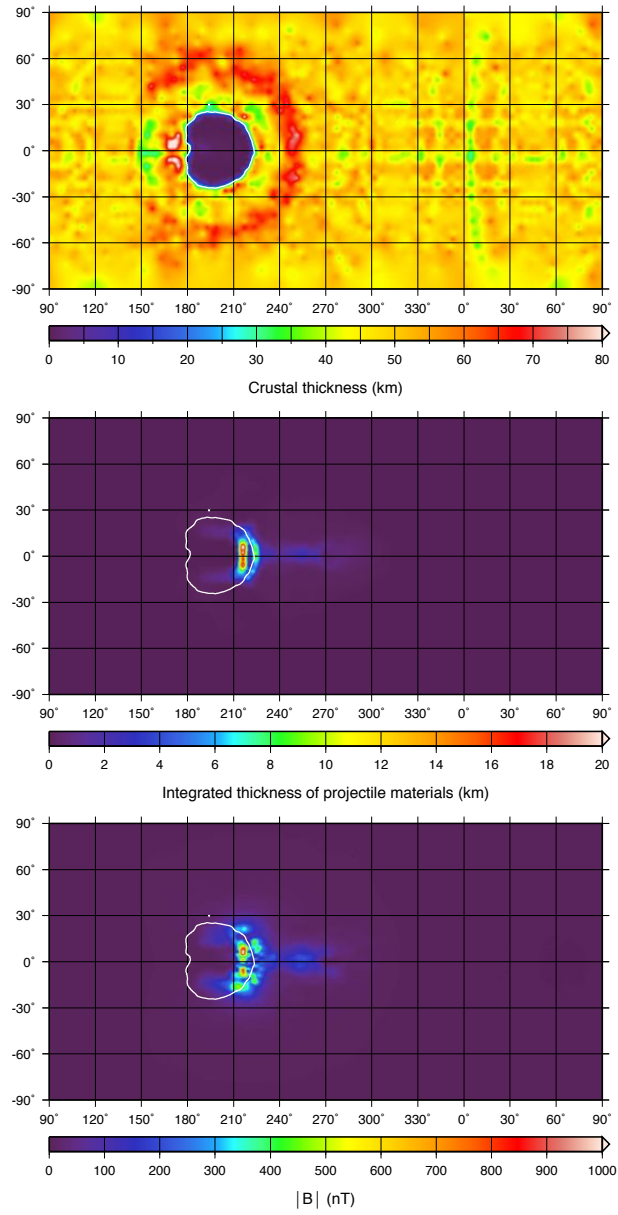
Fig. S8B. Same as Fig. SBA, but for an impact angle of 45° from vertical, a simulation resolution in the crust of 10 km, and 67 minutes following the impact.

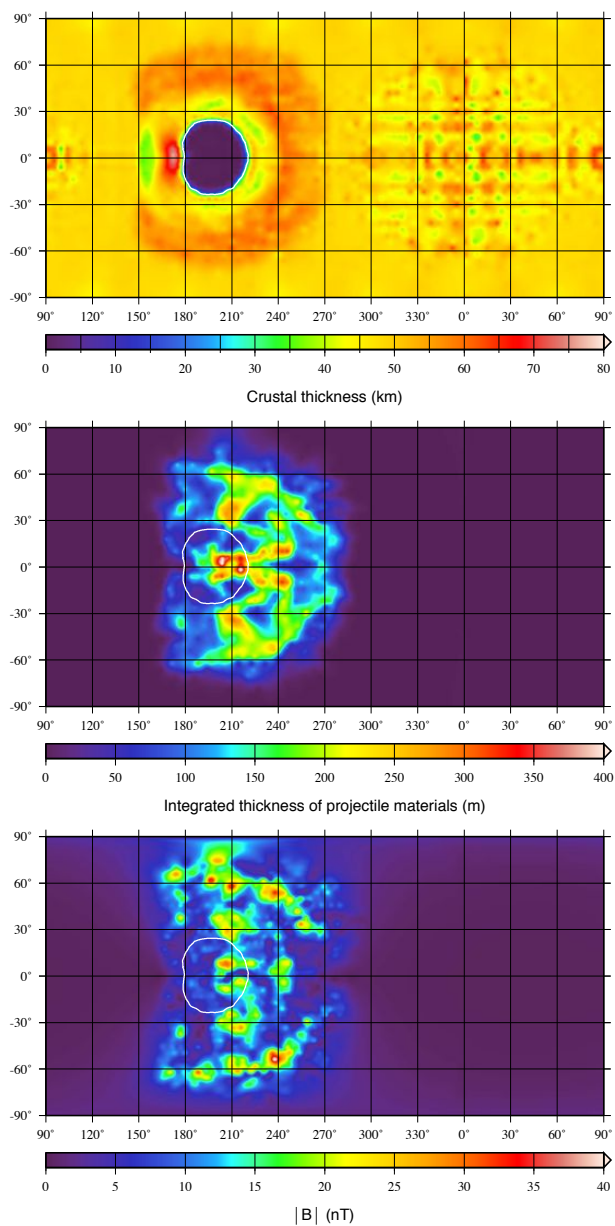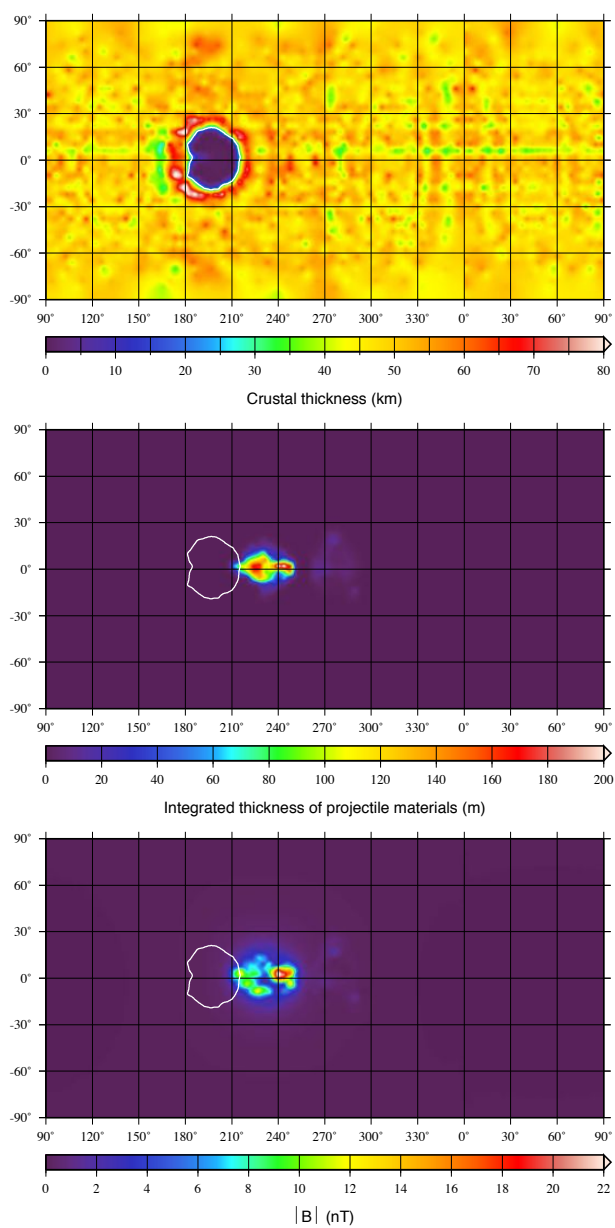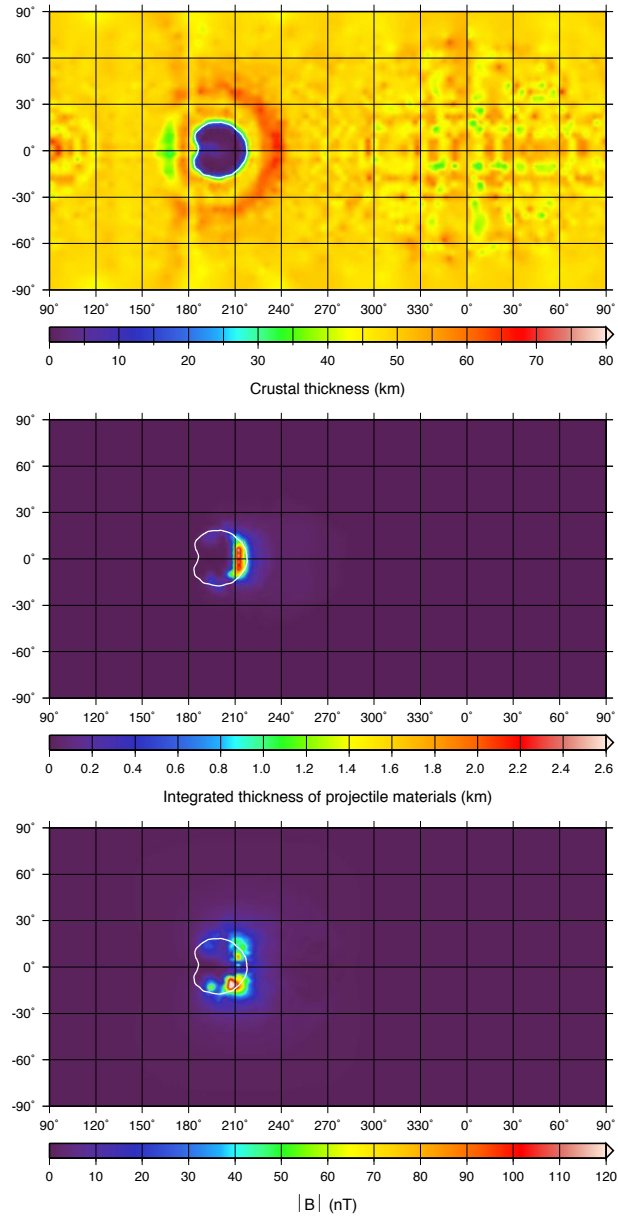**Fig. S8C.** Same as Fig. S8A, but for an impact angle of 60° from vertical, and 67 minutes following the impact.

Table S1. Saturation remanent magnetization per unit mass m_{rs} of lunar rocks in A m^2 kg^{-1}.

Sample number	$\log_{10} m_{rs}$	Source
Mare basalts		
10003	-3.347	*(65)*
10017	-3.108	*(65)*
10020	-2.921	*(65)*
	-3.125	*(66)*
10024	-2.824	*(67,68)*
10047	-3.602	*(65)*
	-3.658	*(69)*
10049	-2.831	*(70)*
10050	-3.137	*(65)*
10057	-2.854	*(65)*
10058	-3.699	*(69)*
10062	-3.222	*(69)*
10069	-1.658	*(65)*
12009	-3.190	*(70)*
12022	-3.357	*(70)*
12053	-3.092	*(67,68,71)*
	-3.602	*(69)*
12063	-3.495	*(69)*
12065	-3.523	*(69)*
	-3.056	*(72)*
15016	-3.155	*(72)*
	-3.367	*(65)*
15058	-3.000	*(68,73)*
15076	-2.076	*(72)*
15495	-3.125	*(73)*
15499	-3.090	*(70)*
	-3.000	*(65)*
15555	-3.000	*(73)*
	-3.456	*(72)*
15556	-2.824	*(73)*
	-2.886	*(73)*
15595	-3.108	*(72)*
15597	-3.342	*(70)*
	-3.409	*(65)*
70017	-2.045	*(74)*
	-3.000	*(75)*
	-2.824	*(75)*
70035	-2.592	*(76)*
	-2.770	*(65)*
70135	-2.745	*(65)*

Sample number	$\log_{10} m_{rs}$	Source
70215	-2.770	(76)
	-2.357	(75)
71055	-2.071	(74)
75055	-3.333	(76)
74275	-2.260	(76)
	-2.112	(74)
78505	-2.721	(65)
79155	-2.387	(65)
NWA 032	-2.852	(19)
NWA 4734	-2.150	(19)
Mg-suite norites		
78235	-2.487	This study, (77)
Mg-suite troctolites		
76535	-3.220	(20)
Pristine anorthosites		
60015	-4.137	(65)
60025	-5.301	(65)
Mafic impact melt breccias		
60315	-3.155	(73)
	-3.071	(78)
61156	-2.523	(75)
	-2.222	(75)
14303	-1.678	(68)
14311	-2.367	(68)
14312	-2.268	(5)
14321	-2.108	(5)
66095	-2.107	(72)
	-2.201	(73)
15455	-2.678	(65)
62235	-1.724	(79)
	-2.180	(65)
65015	-2.602	(65)
77135	-3.086	(65)
14305	-2.553	(65)

Table S2. Summary of magnetic properties of common lunar rocks: sample type, assumed density ρ, saturation remanent magnetization per unit volume M_{rs}, thermoremanence susceptibility χ_{TRM}, and number of samples N.

Sample type	ρ kg m^{-3}	$M_{rs}^{\dagger}$ A m^{-1}	$\chi_{TRM}^{\dagger}$ SI	N
Mafic impact-melt breccias	3000	$11.7\,(+20.8, -7.5)$	$4.92\,(+8.70, -3.14) \times 10^{-3}$	16
Granulitic breccias	2800	$7.02\,(+8.00, -3.74)$	$2.94\,(+3.35, -1.57) \times 10^{-3}$	5
Pristine Mg-suite rocks	3000	$4.20\,(9.77, 1.81)$	$1.76\,(4.09, 0.76) \times 10^{-3}$	2
Mare basalts	3300	$3.77\,(+7.49, -2.51)$	$1.58\,(+3.14, -1.05) \times 10^{-3}$	50
Pristine feldpathic highland rocks	2800	$5.35\,(20.4, 1.40) \times 10^{-2}$	$2.24\,(8.56, 0.59) \times 10^{-5}$	2

[†] Multisample averages and ± 1-σ variability in parentheses calculated assuming a log-normal distribution. When only two samples are available, the values in parenthesis correspond to the minimum and maximum values.

Table S3. Magnetic properties of chondritic and achondritic meteorites: meteorite type, assumed density ρ, saturation remanent magnetization per unit volume M_{rs}, and thermoremanence susceptibility χ_{TRM}.

Meteorite Class	$\rho^{\star}$ kg m^{-3}	$M_{rs}^{\dagger}$ A m^{-1}	$\chi_{TRM}^{\dagger}$ SI	Source
Chondrites				
H	3420	$1160\,(+950, -520)$	$0.485\,(+0.398, -0.219)$	*(80)*
L	3360	$443\,(+805, -286)$	$0.186\,(+0.337, -0.120)$	*(80)*
LL	3220	$950\,(+1277, -545)$	$0.398\,(+0.535, -0.228)$	*(80)*
C(2,4,5)	3530	$401\,(+2767, -350)$	$0.168\,(+1.159, -0.147)$	*(81)*
CI	1600	$1060\,(+30, -30)$	$0.443\,(+0.015, 0.014)$	*(81)*
CK4	2850	$3590\,(+840, -680)$	$1.50\,(+0.35, 0.29)$	*(81)*
CM2	2250	$148\,(+77, -51)$	$0.0619\,(+0.0323, -0.0212)$	*(81)*
CO3	3030	$1530\,(+1710, -810)$	$0.643\,(+0.718, -0.339)$	*(81)*
CR2	3100	$1630\,(+570, -420)$	$0.681\,(+0.238, -0.176)$	*(81)*
CV3	2950	178	0.0745	*(81)*
CV3o	2790	$452\,(+2709, -388)$	$0.190\,(+1.135, -0.162)$	*(81)*
CV3r	3115	$284\,(+1370, -920)$	$1.19\,(+0.57, -0.39)$	*(81)*
EH	3720	$1330\,(+510, -370)$	$0.557\,(+0.213, 0.154)$	*(81)*
EL	3550	$394\,(+299, -170)$	$0.165\,(+0.125, -0.071)$	*(81)*
R	3030$^{\sharp}$	$138\,(+281, -92)$	$0.0577\,(+0.1179, -0.0387)$	*(81)*
Achondrites				
Angrites	3200	$29.7\,(+105.2, -23.1)$	$0.0124\,(+0.0441, -0.0097)$	*(82)*
Aubrites	3120	$7.48\,(+9.48, -4.18)$	$0.00314\,(+0.00397, -0.00175)$	*(82)*
Brachinites	3300	250	0.105	*(82)*
Diogenites	3230	$5.04\,(+5.00, -2.51)$	$0.00211\,(+0.00210, -0.00105)$	*(82)*
Eucrites	2900	$1.57\,(+2.31, -0.94)$	$0.000659\,(+0.000968, -0.000392)$	*(82)*
Howardites	2970	$10.8\,(+9.7, -5.1)$	$0.00452\,(+0.00405, -0.00213)$	*(82)*
Mesosiderites	4250	$985\,(+3349, -761)$	$0.413\,(+1.403, -0.319)$	*(82)*
Ureilites	3050	$1920\,(+2110, -1010)$	$0.806\,(+0.883, -0.421)$	*(82)*

* Densities from *(83–85)*.

† Multisample averages and ± 1-σ variability in parentheses calculated assuming a log-normal distribution.

$^{\sharp}$ Using a density equal to that of CO chondrites.

Table S4. Summary of impact simulations.

Figure number	Impactor diameter, km	Impact velocity, km s^{-1}	Impact angle, degrees	Crust resolution, km	Percent projectile retained[†] mantle	core	EOS table version[♯]
Differentiated impactors							
S1, top	200	15	45	10	(⋆)	90	2
S1, middle	200	15	45	20	4	83	2
S1, bottom	200	15	45	40	4	94	2
S2A	150	30	30	20	0	0.06	2
S2B	150	30	45	20	0.02	0.2	2
—	150	30	60	20	0	0	2
S3A	200	15	30	20	2	100	2
3, S3B	200	15	45	20	0.5	79	2
S3C	200	15	60	20	0	0.7	2
S4A	260	10	30	40	51	100	2
S4B	260	10	45	20	56	71	2
S4C	260	10	60	20	3	18	2
Homogeneous impactors							
S5, top	250	15	45	10	16	—	1
S5, middle	250	15	45	20	11	—	2
S5, bottom	250	15	45	40	13	—	2
S6A	158	30	30	40	3	—	1
S6B	158	30	45	40	0.4	—	1
—	158	30	45	40	0	—	1
S7A	250	15	30	40	79	—	1
S7B	250	15	45	10	16	—	1
S7C	250	15	60	40	1	—	1
S8A	300	10	30	20	74	—	2
S8B	300	10	45	40	36	—	2
S8C	300	10	60	20	5	—	2

[†] Not including retained widely dispersed vaporized materials, which would finely coat the lunar surface.

[♯] The calculations used SESAME-style equations of state (*86*), where pressure and energy are tabulated over a density-temperature grid. Version 2 of the forsterite and silica tables had a finer grid spacing in the vapor region of the phase diagram than version 1.

⋆ Not calculated.

References

1. P. Dyal, C. W. Parkin, W. D. Daily, *Rev. Geophys. Space Phys.* **12**, 568 (1974).

2. L. Hood, *et al.*, *J. Geophys. Res.* **106**, 27,825 (2001).

3. D. L. Mitchell, *et al.*, *Icarus* **194**, 401 (2008).

4. M. E. Purucker, J. B. Nicholas, *J. Geophys. Res.* **115**, E12007 (2010).

5. M. Fuller, S. M. Cisowski, *Geomagnetism*, J. A. Jacobs, ed. (Academic Press, London, 1987), vol. 2, pp. 307–455.

6. J. Gattacceca, *et al.*, *Earth Planet. Sci. Lett.* **299**, 42 (2010).

7. W. D. Daily, P. Dyal, *Phys. Earth Planet. Int.* **20**, 255 (1979).

8. L. L. Hood, Z. Huang, *J. Geophys. Res.* **96**, 9837 (1991).

9. D. Crawford, P. Schultz, *Int. J. Impact Eng.* **23**, 169 (1999).

10. D. R. Stegman, A. M. Jellinek, S. A. Zatman, J. R. Baumgardner, M. A. Richards, *Nature* **421**, 143 (2003).

11. M. A. Wieczorek, *et al.*, *New views of the Moon*, B. J. Jolliff, M. A. Wieczorek, C. K. Shearer, C. R. Neal, eds. (Mineral. Soc. Amer., 2006), vol. 60 of *Rev. Min. Geochem.*, pp. 221–364.

12. M. Le Bars, M. Wieczorek, . Karatekin, D. Cbron, M. Laneuville, *Nature* **479**, 215 (2011).

13. C. Dwyer, D. Stevenson, F. Nimmo, *Nature* **479**, 212 (2011).

14. L. Hood, *Icarus* **211**, 1109 (2011).

15. J. Halekas, R. Lin, D. Mitchell, *Meteorit. Planet. Sci.* **38**, 565 (2003).

16. J. Halekas, *et al.*, *J. Geophys. Res.* **106**, 27,841 (2001).

17. L. Hood, N. Artemieva, *Icarus* **193**, 485 (2008).

18. D. Wang, R. Van der Voo, D. R. Peacor, *Geosphere* **1**, 138 (2005).

19. P. Rochette, J. Gattacceca, A. V. Ivanov, M. A. Nazarov, N. S. Bezaeva, *Earth Planet. Sci. Lett.* **292**, 383 (2010).

20. I. Garrick-Bethell, B. P. Weiss, D. L. Shuster, J. Buz, *Science* **323**, 356 (2009).

21. E. K. Shea, *et al.*, *Science* **335**, 453 (2012).

22. R. L. Korotev, *J. Geophys. Res.* **105**, 4317 (2000).

23. I. Garrick-Bethell, M. T. Zuber, *Icarus* **204**, 399 (2009).

24. R. Tagle, L. Hecht, *Meteorit. Planet. Sci.* **41**, 1721 (2006).

25. R. Tagle, R. T. Schmitt, J. Erzinger, *Geochim. Cosmochim. Acta* **73**, 4891 (2009).

26. R. L. Korotev, *J. Geophys. Res.* **92**, E491 (1987).

27. E. Pierazzo, H. J. Melosh, *Meteorit. Planet. Sci.* **35**, 117 (2000).

28. L. E. Senft, S. Stewart, *Earth Planet. Sci. Lett.* **287**, 471 (2009).

29. A. Brecher, L. Albright, *J. Geomag. and Geoelectr.* **29**, 379 (1977).

30. J. C. Andrews-Hanna, M. T. Zuber, W. B. Banerdt, *Nature* **453**, 1212 (2008).

31. M. M. Marinova, O. Aharonson, E. Asphaug, *Nature* **453**, 1216 (2008).

32. J. E. P. Connerney, *et al.*, *Geophys. Res. Lett.* **28**, 4015 (2001).

33. D. J. Dunlop, J. Arkani-Hamed, *J. Geophys. Res.* **110**, E12S04 (2005).

34. D. E. Smith, *et al.*, *Geophys. Res. Lett.* **37**, L18204 (2010).

35. D. J. Dunlop, K. S. Argyle, *J. Geophys. Res.* **102**, 20199 (1997).

36. P. A. Selkin, J. S. Gee, L. Tauxe, *Earth Planet. Sci. Lett.* **256**, 81 (2007).

37. R. Shaar, *et al.*, *Earth Planet. Sci. Lett.* **290**, 201 (2010).

38. S. K. Runcorn, *Phys. Earth Planet. Inter.* **10**, 327 (1975).

39. G. Kletetschka, M. H. Acuna, T. Kohout, P. J. Wasilewski, J. E. P. Connerney, *Earth Planet. Sci. Lett.* **226**, 521 (2004).

40. J. Gattacceca, P. Rochette, *Earth Planet. Sci. Lett.* **227**, 377 (2004).

41. Y. Yu, *Geochem. Geophys. Geosyst.* **11**, Q02Z12 (2010).

42. T. Kobayashi, J. H. Kim, S. R. Lee, H. Araki, T. Ono, *IEEE Geosci. Remote Sensing Lett.* **7**, 435 (2010).

43. O. Aharonson, M. T. Zuber, S. C. Solomon, *Earth Planet. Sci. Lett.* **218**, 261 (2004).

44. D. A. Varshalovich, A. N. Moskalev, V. K. Khersonskii, *Quantum theory of angular momentum* (World Scientific, Singapore, 1988).

45. J. McGlaun, S. Thompson, M. Elrick, *Int. J. Impact Eng.* **10**, 351 (1990).

46. D. A. Crawford, *Proceedings of the 11th Hypervelocity Impact Symposium*, F. Schafer, S. Hiermaier, eds. (Fraunhofer Verlag, 2011), pp. 693–704.

47. T. Spohn, W. Konrad, D. Breuer, R. Ziethe, *Icarus* **149**, 54 (2001).

48. G. I. Kerley, *Sandia National Laboratory Tech. Rep.* **SAND93-0027** (1993).

49. W. Benz, A. G. W. Cameron, H. J. Melosh, *Icarus* **81**, 113 (1989).

50. H. J. Melosh, *Meteorit. Planet. Sci.* **42**, 2079 (2007).

51. J. R. Rice, *J. Geophys. Res.* **111**, B05311 (2006).

52. R. V. Zucker, S. T. Stewart, *Lunar Planet. Sci. Conf.* **41**, Abstract 2460 (2010).

53. T. Kawazoe, S.-i. Karato, K. Otsuka, Z. Jing, M. Mookherjee, *Phys. Earth Planet. Int.* **174**, 128 (2009).

54. J. Zhang, C. Herzberg, *J. Geophys. Res.* **99**, 17729 (1994).

55. B. A. Ivanov, H. J. Melosh, E. Pierazzo, *Large Meteorite Impacts and Planetary Evolution IV*, R. L. Gibson, W. U. Reimold, eds. (Geol. Soc. Amer., Boulder, CO, 2010), pp. 29–49.

56. S. K. Croft, *J. Geophys. Res.* **88**, B71 (1983).

57. R. M. Iverson, *Rev. Geophys.* **35**, 245 (1997).

58. P. Del Gaudio, *et al.*, *J. Geophys. Res.* **114**, B06306 (2009).

59. D. L. Kohlstedt, *Rev. Mineral. Geochem.* **51**, 121 (2002).

60. I. Garrick-Bethell, F. Nimmo, M. A. Wieczorek, *Science* **330**, 949 (2010).

61. D. A. Morrison, *Lunar Planet. Sci.* **29**, abstract 1657 (1998).

62. M. Le Feuvre, M. A. Wieczorek, *Icarus* **214**, 1 (2011).

63. E. Pierazzo, A. M. Vickery, H. J. Melosh, *Icarus* **127**, 408 (1997).

64. M. A. Wieczorek, M. T. Zuber, *J. Geophys. Res.* **106**, 27,825 (2001).

65. S. M. Cisowski, D. W. Collinson, S. K. Runcorn, A. Stephenson, M. Fuller, *J. Geophys. Res.* **88**, A691 (1983).

66. D. W. Collinson, S. K. Runcorn, A. Stephenson, A. J. Manson, *Proc. Lunar Planet. Sci. Conf.* **3**, 2343 (1972).

67. T. Nagata, R. M. Fisher, F. C. Schwerer, M. D. Fuller, J. R. Dunn, *Proc. Lunar Planet. Sci. Conf.* **2**, 2461 (1971).

68. T. Nagata, R. M. Fisher, F. C. Schwerer, *Moon* **4**, 160 (1972).

69. R. B. Hargraves, N. Dorety, *Proc. Lunar Planet. Sci. Conf.* **2**, 2477 (1971).

70. M. Fuller, E. Meshkov, S. M. Cisowski, C. J. Hale, *Proc. Lunar Planet. Sci. Conf.* **10**, 2211 (1979).

71. J. R. Dunn, M. Fuller, *Moon* **4**, 49 (1972).

72. G. W. Pearce, W. A. Gose, D. W. Strangway, *Proc. Lunar Planet. Sci. Conf.* **4**, 3045 (1973).

73. T. Nagata, R. M. Fisher, F. C. Schwerer, M. D. Fuller, J. R. Dunn, *Proc. Lunar Planet. Sci. Conf.* **4**, 3019 (1973).

74. A. Brecher, W. H. Menke, K. R. Morash, *Proc. Lunar Planet. Sci. Conf.* **5**, 2795 (1974).

75. T. Nagata, *et al.*, *Proc. Lunar Planet. Sci. Conf.* **5**, 2827 (1974).

76. G. W. Pearce, D. W. Strangway, W. A. Gose, *Proc. Lunar Planet. Sci. Conf.* **5**, 2815 (1974).

77. I. Garrick-Bethell, B. P. Weiss, *Lunar Planet. Sci.* **38**, abstract 2405 (2007).

78. A. Brecher, D. J. Vaughan, R. G. Burns, K. R. Morash, *Proc. Lunar Planet. Sci. Conf.* **4**, 2991 (1973).

79. N. Sugiura, D. W. Strangway, *Proc. Lunar Planet. Sci. Conf.* **13**, A684 (1983).

80. P. Rochette, *et al.*, *Meteorit. Planet. Sci.* **38**, 251 (2003).

81. P. Rochette, *et al.*, *Meteorit. Planet. Sci.* **43**, 959 (2008).

82. P. Rochette, *et al*., *Meteorit*. *Planet*. *Sci*. **44**, 405 (2009).

83. D. T. Britt, G. J. Consolmagno, *Meteorit*. *Planet*. *Sci*. **38**, 1161 (2003).

84. G. Consolmagno, D. Britt, R. Macke, *Chemie der Erde / Geochemistry* **68**, 1 (2008).

85. D. T. Britt, R. J. Macke, W. Kiefer, G. J. Consolmagno, *Lunar Planet*. *Sci*. **41**, 1869 (2010).

86. K. Holian, *T-4 handbook of material properties data bases, vol*. *1c: Equations of state*., Report LA-10160-MS (Los Alamos National Laboratory, Los Alamos, NM, 1984).

representations. This does not ultimately settle the question of what neurogenesis in the adult dentate gyrus is good for, but suggests that new neurons are critical for hippocampal function. The functional relevance of adult-born neurons is network-specific, and adult hippocampal neurogenesis is thus distinct from the only other neurogenic region of the adult brain, the olfactory bulb. The healthy dentate gyrus turns out to be a house for many generations of cells under one roof and the site of an intriguing collaboration between the young and the older.

References

1. A. Marín-Burgin, L. A. Mongiat, M. Belén, A. F. Schinder, *Science* **335**, 1238 (2012); 10.1126/science.1214956.
2. H. Schwegler, W. E. Crusio, I. Brust, *Neuroscience* **34**, 293 (1990).
3. H. Schwegler, H. P. Lipp, H. Van der Loos, W. Buselmaier, *Science* **214**, 817 (1981).
4. J. B. Aimone, W. Deng, F. H. Gage, *Trends Cogn. Sci.* **14**, 325 (2010).
5. G. Kempermann, in *Adult Neurogenesis 2–Stem Cells and Neuronal Development in the Adult Brain*, G. Kempermann, Ed. (Oxford Univ. Press, New York, 2011).
6. L. A. Mongiat, A. F. Schinder, *Eur. J. Neurosci.* **33**, 1055 (2011).
7. G. Kempermann, *J. Neurosci.* **22**, 635 (2002).
8. N. Kee, C. M. Teixeira, A. H. Wang, P. W. Frankland, *Nat.* *Neurosci.* **10**, 355 (2007).
9. A. Tashiro, V. M. Sandler, N. Toni, C. Zhao, F. H. Gage, *Nature* **442**, 929 (2006).
10. C. Schmidt-Hieber, P. Jonas, J. Bischofberger, *Nature* **429**, 184 (2004).
11. J. S. Snyder, N. Kee, J. M. Wojtowicz, *J. Neurophysiol.* **85**, 2423 (2001).
12. S. Ge, C. H. Yang, K. S. Hsu, G. L. Ming, H. Song, *Neuron* **54**, 559 (2007).
13. M. D. Saxe et al., *Proc. Natl. Acad. Sci. U.S.A.* **103**, 17501 (2006).
14. A. Garthe, J. Behr, G. Kempermann, *PLoS ONE* **4**, e5464 (2009).
15. C. B. Alme et al., *Hippocampus* **20**, 1109 (2010).

GEOCHEMISTRY

Moonstruck Magnetism

Do magnetic anomalies on the Moon indicate the remains of a giant asteroid impact?

Gareth S. Collins

A surprising result of the Apollo missions was the discovery of strong, localized magnetic fields emanating from the lunar crust (*1*). One reason these fields are so enigmatic is that endogenous lunar rocks contain a low abundance of metallic iron, making them very weakly magnetic (*2*–*4*). How, then, did the Moon record such strong magnetic signatures? On page 1212 of this issue, Wieczorek et al. (*5*) propose that many of the Moon's magnetic anomalies originate from highly magnetic deposits of a giant asteroid that collided with the Moon early in its history. These readily magnetized, extralunar deposits subsequently recorded magnetic fields that may have been generated by an ancient lunar core dynamo and/or transient impact-generated fields.

The generation of a magnetic anomaly requires two things—a magnetic field and a magnetic mineral that will record it. On Earth, the principal magnetic minerals are iron oxides and sulfides produced in the oxidizing terrestrial environment. By contrast, in the reducing lunar environment, metallic iron-nickel alloys are the main carriers of remanent magnetization. Meteoritic materials can contain magnetic minerals of both types. Whereas magnetic minerals are generally abundant in meteoritic material, they are extremely rare in the Moon's crust and upper mantle because of the nature of the Moon's formation and its thermal evolution. As a result, endogenous lunar materials are very poor at recording magnetic fields, whereas meteoritic material can be orders of magnitude more magnetic. Wieczorek et al. use this observation to show that the strength of the lunar magnetic anomalies would require unrealistically thick deposits of unidirectionally magnetized lunar crustal materials, but can be explained by relatively thin deposits of meteoritic material.

On the basis of the observation that the spatial distribution of many of the anomalies corresponds to the northern "rim" of the mammoth South Pole–Aitken (SPA) impact basin on the far side of the Moon, ~2500 km in diameter (*6*), Wieczorek et al. go on to propose that deposits from the SPA impactor are the source materials for the lunar magnetic anomalies. According to their hypothesis, the SPA impactor was ~200 km in diameter, approached the Moon from the south, and collided at an oblique angle to form an elongated crater. In the process, impactor debris was sprayed downrange to the north and deposited near the northern basin rim. Computer simulations of SPA-scale impacts performed to test this hypothesis predict final impactor deposits that can explain the observed strength and distribution of many of the Moon's magnetic anomalies.

Wieczorek et al.'s innovation explains where the Moon's main magnetic field recorders came from, but what was the source of the ancient magnetic fields? Evidence for an iron core in the Moon that is currently at least partially molten (*7*) suggests that one possibility is an ancient lunar dynamo. Support for this
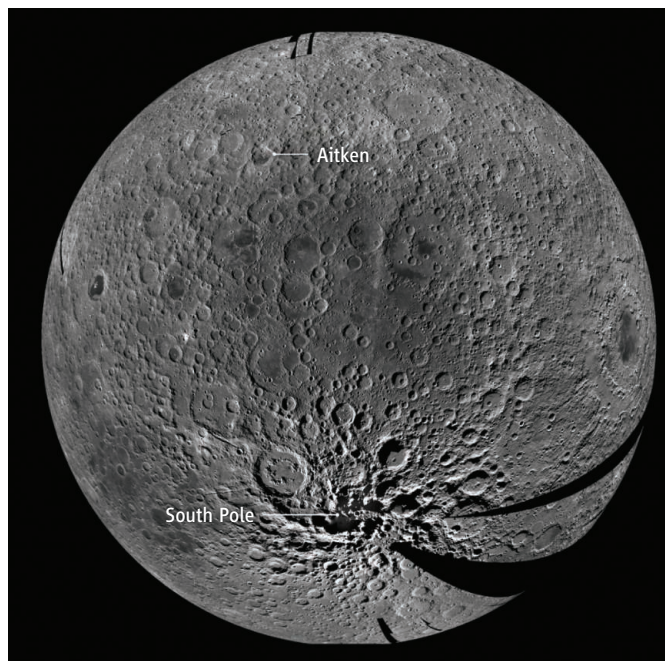
Making an impact. The South Pole–Aitken basin on the far side of the Moon, the largest and oldest definitive impact crater in the solar system, spans more than one-quarter of the Moon's circumference from Aitken crater in the north to the lunar South Pole. This image is a mosaic from the Lunar Reconnaissance Orbiter Camera (LROC) Wide Angle Camera (WAC).

Department of Earth Science and Engineering, Imperial College London, London SW7 2AZ, UK. E-mail: g.collins@imperial.ac.uk

idea comes from paleomagnetic analyses of lunar samples (8–10), which suggest that an ancient lunar magnetic field, comparable in intensity to Earth's present field, persisted for several hundred million years. This long duration is difficult to explain by an Earth-like dynamo driven by thermal or chemical convection (11), but recent work has revived the idea, suggesting that an ancient lunar dynamo could have been powered by differential rotation between the Moon's core and mantle, either continuously over several hundred million years (12) or for short periods after giant impacts (13). Broad magnetic anomalies over several Nectarian-aged (from 3.92 to 3.85 billion years ago) impact basins, recorded by slow cooling over long time periods, are also evidence for an early lunar core dynamo (14). However, it is also possible that the highly magnetic impactor remnants were magnetized by transient impact-generated fields (6) long after they were deposited. As these ephemeral fields are strongest at the impact antipode, this idea explains the intriguing correlation between some of the largest magnetic anomalies and the antipodes

of the four largest young impact basins on the Moon (15).

As the largest and oldest impact crater in the solar system, the SPA basin is of immense importance and is a strong candidate location for future sample-return missions. Although the detailed geologic record of Earth's formative past was erased long ago, the Moon preserves materials in its crust and mantle that date from before continents grew and life began to stir on Earth. The huge SPA impact brought deep lunar materials to the surface, and sampling these otherwise inaccessible rocks could hold the key to understanding how the Earth-Moon system formed and evolved. Moreover, an accurate absolute age for the basin would provide a vital anchor for interpreting the violent bombardment history of the Earth and Moon and its influence on the evolution of life on Earth. If Wieczorek et al.'s hypothesis is correct, a sample-return mission to SPA's northern rim may also uncover ancient meteoritic material from the giant asteroid that formed the basin itself. And if this highly magnetic material is accessible,

it could prove an invaluable resource for human colonization of the Moon.

References
1. P. Dyal, C. W. Parkin, C. P. Sonett, *Science* **169**, 762 (1970).
2. M. Fuller, S. M. Cisowski, *Geomagnetism* **2**, 307 (1987).
3. K. Lawrence, C. Johnson, L. Tauxe, J. Gee, *Phys. Earth Planet. Inter.* **168**, 71 (2008).
4. P. Rochette, J. Gattacceca, A. V. Ivanov, M. A. Nazarov, N. S. Bezaeva, *Earth Planet. Sci. Lett.* **292**, 383 (2010).
5. M. A. Wieczorek, B. P. Weiss, S. T. Stewart, *Science* **335**, 1212 (2012).
6. L. L. Hood, N. A. Artemieva, *Icarus* **193**, 485 (2008).
7. R. C. Weber, P.-Y. Lin, E. J. Garnero, Q. Williams, P. Lognonné, *Science* **331**, 309 (2011).
8. I. Garrick-Bethell, B. P. Weiss, D. L. Shuster, J. Buz, *Science* **323**, 356 (2009).
9. S. M. Cisowski, D. W. Collinson, S. K. Runcorn, A. Stephenson, M. Fuller, *J. Geophys. Res.* **88**, A691 (1983).
10. E. K. Shea et al., *Science* **335**, 453 (2012).
11. D. R. Stegman, A. M. Jellinek, S. A. Zatman, J. R. Baumgardner, M. A. Richards, *Nature* **421**, 143 (2003).
12. C. A. Dwyer, D. J. Stevenson, F. Nimmo, *Nature* **479**, 212 (2011).
13. M. Le Bars, M. A. Wieczorek, O. Karatekin, D. Cébron, M. Laneuville, *Nature* **479**, 215 (2011).
14. L. L. Hood, *Icarus* **211**, 1109 (2011).
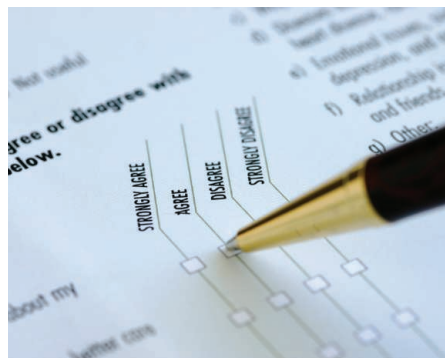15. R. P. Lin, K. A. Anderson, L. L. Hood, *Icarus* **74**, 529 (1988).

SOCIAL SCIENCE

Experimenting with Politics

Social scientists are turning increasingly to experiments to explain important political behaviors.

James N. Druckman[1] and Arthur Lupia[2]

In his 1909 presidential address to the American Political Science Association, A. Lawrence Lowell (1) advised the then-fledgling discipline against following the natural scientists into greater use of experimental designs. This attitude toward experiments was still dominant at the end of the World War II, when political scientists were using increasingly intricate statistical methods to characterize relationships, but still ran few experiments. The tide began to turn in the 1980s, when scholars started to integrate the accumulated knowledge of traditional political science with the theoretical approaches of psychology and economics. This trend generated more acute causal predictions, which, along with technological developments, led political scientists to increasingly turn to experiments. Today, experiments are often the preferred method

to explain the causes and consequences of political behaviors (2).

Political scientists commonly use three different experimental methods. Laboratory experiments place subjects in situations that show how people reach decisions as voters, jurors, or legislators. Political scientists also embed experiments in large, and often nationally representative, surveys. These

Your opinion counts. In survey experiments, political scientists explore how the attitudes, perceptions, and emotions of citizens affect their responses in opinion surveys.

experiments elucidate how variations in the descriptions or presentations of political phenomena affect the perceptions and feelings of diverse citizen populations. Finally, in field experiments, researchers integrate random assignment into real political campaigns or attempts to implement policy. These experiments can clarify the relative effectiveness of various tactics and strategies.

Laboratory experiments can, for example, inform the design and effectiveness of governmental institutions. In a classic laboratory experiment by Ostrom et al. (3), each subject decided how much to withdraw from a group fund that mimicked a scarce environmental resource. If the subjects overwithdrew, then the group as a whole earned less. Allowing group members to shame those who overwithdrew, or to shame and fine, yielded greater collective benefits than did fines alone. The results challenged the long-standing presumption that a group's ability to produce high-value public goods—such as good air quality for all, despite individual incentives to pollute—requires an external author-

[1]Department of Political Science and Institute for Policy Research, Northwestern University, Evanston, IL 60208, USA. [2]Department of Political Science and Institute for Social Research, University of Michigan, Ann Arbor, MI 48104, USA. E-mail: druckman@northwestern.edu; lupia@isr.umich.edu